Parallel organization of cerebellar pathways to sensorimotor, associative, and modulatory forebrain

Thomas J. Pisano[1*], Zahra M. Dhanerawala[1*], Mikhail Kislin[1], Dariya Bakshinskaya[1], Esteban A. Engel[1], Junuk Lee[1], Nina L. de Oude[2], Ethan J. Hansen[3], Kannan Umadevi Venkataraju[4], Freek Hoebeek[5], Ben D. Richardson[3,6,] Jessica L. Verpeut[1], Henk-Jan Boele[1**], and Samuel S.-H. Wang[1**]

[1]Neuroscience Institute, Washington Road, Princeton University, Princeton, NJ 08544 USA.
[2]Department of Neuroscience, Erasmus MC, 3000 DR Rotterdam, The Netherlands.
[3]WWAMI Medical Education, University of Idaho, Moscow, ID 83844 USA.
[4]Cold Spring Harbor Laboratory, One Bungtown Road, Cold Spring Harbor, NY 11724 USA.
[5]Heidelberglaan 100, University Medical Center Utrecht, Utrecht, The Netherlands.
[6]Department of Pharmacology, Southern Illinois University School of Medicine, Springfield, IL 62794 USA.

*Contributed to this work equally.
**Corresponding authors.

Correspondence: Samuel S.-H. Wang
Neuroscience Institute, Washington Road
Princeton University
Princeton, New Jersey 08544 USA
sswang@princeton.edu
+1 (609) 258-0388

Henk-Jan Boele
Neuroscience Institute, Washington Road
Princeton University
Princeton, New Jersey 08544 USA
hboele@princeton.edu
+1 (609) 510-3154

Abstract

Cerebellar outputs take almost exclusively polysynaptic routes to reach the rest of the brain, impeding conventional tracing efforts. Here we quantify pathways between cerebellar cortex and contralateral thalamic and corticostriatal structures using an anterograde (H129) transsynaptic tracer herpes simplex virus type 1, a retrograde (Bartha) tracer pseudorabies virus, and a whole-brain pipeline for neuron-level analysis using light-sheet microscopy. In ascending pathways, sensorimotor regions contained the most labeled neurons, but higher densities were found in associative areas, including orbital, anterior cingulate, prelimbic, and infralimbic cortex. Ascending paths passed through most thalamic nuclei, especially ventral posteromedial and lateral posterior (sensorimotor), mediodorsal (associative), and reticular (modulatory) nuclei. Retrograde tracing revealed that the majority of descending paths originate from somatomotor cortex. Patterns of ascending influence correlated with anatomical pathway strengths, as measured by brainwide mapping of c-Fos responses to optogenetic inhibition of Purkinje cells. Our results reveal parallel functional networks linking cerebellum to forebrain and suggest that cerebellum is capable of using sensory-motor information to guide both movement and nonmotor functions.

INTRODUCTION

The cerebellum has an increasingly recognized role in nonmotor processing[1–3]. Patients with cerebellar damage show multiple cognitive and affective symptoms[1], and damage at birth leads to autism spectrum disorder (ASD) in half of cases[4–6]. These observations suggest a broad role for the cerebellum in nonmotor function during development and adulthood.

However, the pathways that mediate these influences are poorly characterized on a whole-brain scale. Of particular interest is the cerebellum's partnership with neocortex as these

two structures are the second-largest and largest divisions, respectively, of most mammalian brains[7]. The major descending corticocerebellar pathway passes through the pons and the majority of returning ascending fibers pass through the thalamus[8,9], comprising two massive within-brain long-distance pathways[10]. These descending and ascending pathways are suggested to form closed loops[11], giving each cerebellar region one or more specific neocortical partners with which it exchanges information.

Great efforts have been made in mapping the structure of inputs, organization, and outputs of the cerebellum. Two information streams, originating from the cortex and spinal cord, serve as input into the cerebellum, with their targets arranged in zones defined by gene expression and climbing fiber connections[12–15]. Incoming information through the mossy fiber/granule-cell pathway diverges massively, followed by convergence onto Purkinje cells and deep cerebellar nuclei (DCN)[13]. However, although classic tracing methodology can label monosynaptic connections along these paths, the same methods cannot trace incoming or outgoing polysynaptic chains of connection.

Given the brain-wide nature of cerebello-cortical pathways, researchers have examined them using large-scale functional approaches. Transcranial magnetic stimulation in humans has demonstrated that the cerebellum influences neocortical excitability[16]. Functional MRI can attain subcentimeter resolution, detect long-distance correlations[17], and when coupled with cerebellar stimulation in mice, demonstrate causal relationships[18]. Rat cerebellar output to focal regions in the sensorimotor cortex and primate cerebellar output to specific motor and nonmotor regions have been mapped by transsynaptic tracers[19,20]. Functional imaging at cellular resolution in nonhuman animals has been made possible by visualizing c-Fos, an immediate-early gene product whose expression is regulated by neural activity. Although useful in demonstrating coupling between distant brain regions, these methods do not provide cellular-resolution information about cerebello-cortical circuits.

50 Pathways entering and exiting the cerebellum pass through synapses in the brainstem
51 and the cerebellum itself, blocking the passage of most cellular tracer molecules. However, this
52 problem can be overcome using transsynaptically transported viruses[21]. The H129 strain of
53 herpes simplex virus type 1 (HSV-H129) is an anterograde tracer that can identify long-distance
54 targets of specific brain regions. For retrograde tracing, the Bartha strain of pseudorabies virus
55 (PRV-Bartha) allows efficient synapse-specific transport. Thus recent molecular technology
56 opens a means of mapping the cerebellum to its brainwide information-processing partners.
57 Conventional histological methods are too laborious for quantifying connectivity in the
58 whole brain at once. But with the recent advent of optimized tissue clearing techniques with light-
59 sheet microscopy[22], the same tracing methods can now be scaled to cover entire brains. The
60 resulting imaging datasets can occupy terabytes, creating a need for computationally efficient cell
61 detection and anatomical assignment. These challenges can be addressed using machine
62 learning algorithms to detect neurons and image registration methods to align brains. For the
63 cerebellum, an additional problem is the absence of a reference template: the current field
64 standard, the Allen Brain Atlas, omits the posterior two-thirds of the cerebellum. Any integrative
65 study of cerebellar anatomy and function must therefore start with the creation of a suitable atlas.
66 In this project we used HSV-H129 to map the cerebellum's direct ascending outputs to the
67 thalamus and striatum and trisynaptic paths to the neocortex, and PRV-Bartha to map descending
68 paths from neocortex to cerebellum. We then used these measurements to generate a brainwide
69 atlas of cerebellum-forebrain connectivity. We developed an analysis pipeline that allows per-
70 region cell counts to be converted from cell counts to per-volume cell density, giving a measure
71 of relative impact on local circuitry. The potential impact of ascending paths was confirmed using
72 optogenetic stimulation of c-Fos expression. All measurements were referred to a whole-brain
73 atlas that includes the entire cerebellum. Taken together, our results provide a brainwide
74 quantitative map of the cerebellum's connectivity partners and provide insight into the extent of

75 divergence and convergence in pathways between neocortex and cerebellum, as well as possible
76 cerebellar contributions to whole-brain function and neurocognitive disorders.

RESULTS

77 HSV-H129 transsynaptic viral labeling reveals distant cerebellar targets

78 To trace transsynaptic pathways from cerebellum to midbrain and neocortex, we used
79 HSV-H129-VC22 (**Figure 1a**), an HSV-H129 recombinant virus that expresses enhanced green
80 fluorescent protein (EGFP) targeted by means of a localization sequence to the cell nucleus.
81 Transsynaptic viral tracing yields weaker labeling of cells compared with longer-expression-time
82 strategies such as AAV-driven fluorophore expression. To achieve a high signal-to-noise ratio we
83 used iDISCO+, a method that combines tissue clearing, whole-brain immunostaining using Dako
84 anti-HSV antibody, and light-sheet microscopy.

85 To determine the optimal timepoints for examining primarily disynaptic (*i.e.* Purkinje cell
86 to cerebellar nuclear to thalamic) and primarily trisynaptic (Purkinje cell to cerebellar nuclear to
87 thalamic to neocortical) targets, we injected H129-VC22 into the cerebellar cortex of mice and
88 examined tissue between 12 and 89 hours post-injection (hpi; **Figure 1b,c**). At 54 hpi, labeling
89 was observed in thalamus, with little visible labeling in neocortex (**Figure 1c,d**), and we used this
90 as the thalamic timepoint (**Table 1**). Labeling was seen in other midbrain and hindbrain areas,
91 consistent with known monosynaptic anterograde targets of the cerebellar and vestibular
92 nuclei[23,24]. Neocortical labeling was first visible at 73 hpi and throughout its extent by 82 hpi; we
93 defined 80 hpi as our neocortical timepoint. These timepoints are consistent with prior studies
94 using transsynaptic tracing with conventional histological-sectioning methods spanning two
95 synapses (60-72 hpi; Refs. 2,25; **Table 6**) and three synapses (80-96 hpi; Refs. 2,25).

96 HSV-H129 has previously been reported to have a slow retrograde component[26], which
97 might occur via uptake by axon terminals[27] followed by transport backward across synapses. To

98 test this, we examined dorsal column nuclei, which are two synaptic steps retrograde from the
99 cerebellar cortex (via mossy fibers) but which receive no known cerebellar-nuclear or vestibular-
100 nuclear innervation (**Supplementary Figure 1**). At 28-36 hpi, HSV-H129 led to minimal visible
101 labeling in the dorsal column nuclei). We normalized injections by dividing cell density by
102 anterogradely labeled cell density in the DCN. The retrograde:anterograde density ratio for HSV-
103 H129 injections was a median of 0.084 ± 0.032 at 28-36 hpi (estimated SEM, n=15 locations in 5
104 mice), and 0.096 ± 0.017 at 54 hpi (n=69 locations in 23 mice). To demonstrate the maximum
105 possible amount of retrograde labeling we used PRV (80 hpi) and found a median
106 retrograde:anterograde density ratio of 2.06 ± 0.17 (n=75 locations in 25 mice). Finally, we
107 ascertained where any retrograde HSV-H129 viral uptake would lead via subsequent anterograde
108 spread by examining the Mouselight database[28] (http://ml-neuronbrowser.janelia.org/). We found
109 36 fully-traced brainstem (medulla and pons) neurons with at least one axon projecting into the
110 cerebellum. In all but one of these neurons, the cerebellum was the sole target (**Supplementary**
111 **Figure 2**). Thus, to the extent that retrograde transport from injection sites occurs, it would still
112 not lead to alternate noncerebellar pathways. For purposes of transsynaptic tracing we conclude
113 that at our selected timepoints, HSV-H129 acts as an anterograde tracer.

114 **Automated cell detection using a convolutional neural network**

115 Each brain generated a dataset exceeding 100 gigabytes. To automate cell detection, we
116 trained a three-dimensional convolutional neural network (CNN) to recognize neurons. A CNN
117 with U-Net architecture running on a GPU-based cluster was trained by supervised learning using
118 more than 3600 human-annotated centers of cells as ground truth (**Figure 1e**; **Table 2**). The
119 performance at different likelihood thresholds was plotted as a receiver-operator curve of
120 precision and recall (**Figure 1f**), where precision was defined as the number of true positives
121 divided by all positives, and recall was defined as the number of true positives divided by the

number of true positives plus false negatives. A threshold likelihood of 0.6 was found to maximize the harmonic mean of precision and recall, a quantity known as the F1 score. Querying the CNN with the testing dataset gave an F1 score of 0.864, nearly the F1 score for human-human concordance, 0.891, indicating that the CNN had successfully generalized to whole-brain datasets.

Generation of the Princeton Mouse Atlas

To overcome past difficulties in registering images taken using different modalities, we devised a two-step procedure to calculate an averaged light-sheet-based brain template for referral to the Allen Brain Atlas (**Figure 2**). After this procedure, we fitted individual light-sheet brains to this template. The Allen Brain volumetric Atlas (ABA), a field standard, is based on serial two-photon microscopy and lacks a complete cerebellum (**Figure 2a**). To remedy that lack and to generate a template useful for our light-sheet images, we constructed a Princeton Mouse brain Atlas (PMA; **Supplementary Figure 3**). To make the PMA compatible with Allen standards, we computed a transform to convert it to Allen Brain CCFv3 space (**Figure 2b**). We then extended the space using manually-drawn contours to generate a complete, annotated cerebellar anatomy (**Figure 2c,d**) that included posterior lobules (**Figure 2c,d** red lines; **Supplementary Figure 4**).

To quantify the precision of atlas registration, we asked blinded users to find readily identifiable points in our atlas, in four sets of unregistered, affine-only registered, and fully registered volumes (**Figure 2b**, **Supplementary Figure 5**). After registration, the median Euclidean distance from complementary points in the PMA was 93 ± 36 μm (median ± estimated standard deviation) to b-spline registered volumes. Blinded users determined points in the same volume twice to establish an intrinsic minimum limit of 49 ± 40 μm. Assuming that uncertainties sum as independent variables, the estimated accuracy of the registration method was $\sqrt{(93^2-49^2)}$=79 μm, or 4 voxels.

146 **The cerebellum sends output to a wide range of thalamic targets**

147 We used our automated analysis pipeline, which we named BrainPipe, to quantify
148 cerebello-thalamic connectivity (**Figure 3a**). We injected 23 brains with H129-VC22 at different
149 sites in the posterior cerebellum (**Figure 3b; Supplementary 6,7**) and collected brains at 54 hpi,
150 the thalamic timepoint. At this time, the number of neurons per region were widely distributed
151 among contralateral thalamic regions (**Figure 3c**). The density of neurons observed in neocortical
152 regions was 0.085 ± 0.073 (mean ± standard deviation, 17 regions) times that seen in 80 hpi
153 injections, indicating that sufficient time had elapsed to allow transport to thalamus but not to
154 neocortex. Number of neurons by region were not systematically related to anteroposterior
155 position (rank correlation with anteroposterior position r=+0.05), suggesting that the efficiency of
156 labeling was not strongly dependent on differences in transport distance. For display, the number
157 of neurons for each region were converted to percentage of total per-brain thalamic neurons and
158 coded according to "sensory/motor" and "polymodal association" functionalities based on ABA
159 ontology (**Figure 3,** yellow/green shading).

160 The cerebellothalamic tract originates from the cerebellar nuclei and ascends through the
161 superior cerebellar peduncle (also known as brachium conjunctivum), with most axons crossing
162 the midline before reaching the thalamus. We observed vestibular nuclear labeling after cerebellar
163 cortical injections, consistent with a direct projection from the cerebellar cortex (**Supplementary**
164 **Figure 8)**. Short-incubation experiments showed that vestibular nuclei contained 22% of the total
165 combined vestibular and cerebellar-nuclear cell count. To assess the contribution of these paths
166 to vestibular nuclei, we examined the Mouselight database[28] and found 9 Purkinje cells with direct
167 vestibular-projecting axons, 6 of which were found in non-flocculonodular regions
168 (**Supplementary Figure 8)**. Thus a substantial fraction of cerebellar projections to vestibular
169 nuclei arise from widely distributed lobules.

170 A principal target of cerebellothalamic axons is the thalamic ventral nuclear group[23,29],
171 which include somatosensory and somatomotor nuclei[30]. Consistent with known DCN projections,
172 we observed strong connectivity to ventromedial (VM) and ventral anterior-lateral (VAL), motor
173 thalamic nuclei[31], from vermal lobules (I-VII) and Crus II, and moderate connectivity from Crus I
174 (**Figure 3d,e**). The ventral posteromedial nucleus (VPM), which conveys somatosensory whisker
175 and mouth information, received diverse input from all but the most extreme posterior cerebellar
176 areas (**Figure 3c,d,e**) consistent with known interpositus and vestibular nuclear projections[24,32].
177 These findings confirm that cerebellar-injected H129-VC22 labels major known pathways to
178 neocortex via multiple distributed cerebellar-nuclear, vestibular, and thalamic intermediates.

179 We also observed labeling outside the ventral thalamus, including the thalamic reticular
180 nucleus (TRN), lateral posterior (LP) and mediodorsal (MD) nuclei, and zona incerta[33]. MD and
181 LP are association thalamic nuclei. MD is engaged during reversal learning[34], sends its output to
182 frontal regions, including insular, orbital, and prelimbic cortex[35], and is engaged in cognitive and
183 working memory tasks in humans[34]. Lobule VI, a site of structural abnormality in ASD[36], made
184 dense projections to MD (**Figure 3d,e**). These results suggest a strong role for cerebellum in
185 flexible cognition. LP sends its output to primary somatosensory cortex, primary and secondary
186 motor cortex, and frontal association area[35]. TRN, unlike other thalamic nuclei, does not project
187 to neocortex, instead sending inhibitory projections to other thalamic nuclei. Thus, major paths
188 from cerebellum to thalamus include both relay nuclei and the other two major classes of nuclei,
189 association (MD, LP) and local modulatory (TRN).

190 To identify specific topographical relationships, we fitted a generalized linear model (GLM;
191 **Figure 3d**), using the fraction-by-lobule of the total cerebellar injection as input parameters, and
192 the fraction-by-nucleus of total thalamic expression as output measurements. The GLM revealed
193 a broad mapping of lobules I-X to a variety of thalamic targets, and a more focused pattern of
194 mapping from simplex, crus I and II, paramedian lobule, and copula pyramidis to specific thalamic
195 targets. Hotspots of mapping included lobules I-X to VPM, TRN, MD, VM, VPL, VA-L,

196 paraventricular, anteromedial, and centrolateral; simplex to VPM, LP, dorsal lateral geniculate,
197 medial geniculate, and anterodorsal; crus I to VPM, lateral dorsal, reuniens, paraventricular and
198 anteromedial and central lateral; crus II to zona incerta, VPM, MD, TRN, VA-L, posterior complex,
199 and LP; and paramedian lobule and copula pyramidis to zona incerta, LD, parafascicular, ventral
200 lateral geniculate, and lateral habenula (**Table 3**).

201 **Direct projections from cerebellar nuclei to thalamus are largely consistent with**
202 **transsynaptic tracing**

203 As a second, non-transsynaptic approach to characterizing cerebellar projections to thalamus, we
204 injected adeno-associated virus containing the GFP sequence into cerebellar nuclei and
205 characterized the spatial distribution of fluorescent nerve terminals (**Figure 4**). Injections (n=4) of
206 125 nl (titer 7×10^{12} vg/mL) primarily targeted bilateral dentate nuclei and also reached interposed
207 and fastigial nuclei (**Figure 4a; Supplementary Figure 9**). Three weeks after injection, animals
208 were sacrificed and brains sectioned and imaged by confocal microscopy (**Figure 4b**).
209 Terminals were clearly visible throughout thalamic sites, largely contralateral to the site of
210 injection. Counts of vGluT2 and YFP co-labeled varicosities in thirteen randomly picked regions
211 in VM, VA-L, and CL (each region 100x100x5 microns) were strongly correlated with average
212 YFP brightness for that same region ($r=+0.94$, $t=8.76$, $p<0.0001$; **Supplementary Figure 10**).
213 Therefore we used summed brightness as a measure of total innervation. Summed brightness
214 was defined as the total fluorescence within a nucleus, summed across all sections where the
215 nucleus was present. Overall, the highest summed brightness was found in ventral thalamic nuclei
216 including VM, VA-L, VPM, and VPL, consistent with previous literature reports and with the density
217 of cells observed in HSV-H129 injections. The nucleus-by-nucleus fluorescence density (*i.e.*
218 summed brightness divided by the total area covered by the nucleus in the analyzed images) was
219 correlated with the HSV-H129 neuron density averaged across all injections (**Figure 4c**; log-log

220 correlation r=+0.59, p=0.023). Taken together, these measurements indicate that HSV-H129
221 injections at the thalamic timepoint capture a representative pattern of projection from cerebellar
222 nuclei to contralateral thalamus.

223 **Cerebellar nuclei project directly to the reticular thalamic nucleus**

224 To identify neurons forming a monosynaptic projection to TRN, we injected into the TRN an
225 adeno-associated virus (AAV) that infects presynaptic terminals and expressed retrogradely
226 along axons to the parent neuronal cell body (AAVrg; Ref. 37). Injection into TRN of AAVrg-hSyn-
227 Chronos-GFP[38] induced GFP expression in a subset of neurons contralateral to the injection in
228 the ventrolateral dentate and dorsolateral interpositus nuclei (**Figure 4d-g; Supplementary**
229 **Figure 11**), consistent with prior reports[39–41] (**Supplementary Figure 12**). This pattern of
230 retrograde labeling in the cerebellar nuclei using a non-transsynaptic viral tracer (AAVrg) supports
231 the thalamic-timepoint HSV labeling data which indicate a direct projection from cerebellar nuclei
232 to TRN. An injection that missed TRN and instead infected nearby internal capsule
233 (**Supplementary Figure 11**) did not label neurons in cerebellar nuclei. In summary, AAVrg-based
234 retrograde labeling from TRN confirms a monosynaptic projection from cerebellar nuclei and is
235 consistent with the disynaptic projection from cerebellar cortex uncovered by HSV-H129
236 injections.

237 **Cerebellar paths to neocortex are strongest in somatomotor regions and densest in frontal**
238 **regions**

239 To characterize cerebellar paths to neocortex, we examined 33 HSV-injected brains at 80
240 hpi (**Figure 5a,b,c**). As expected, the majority of contralateral neocortical neurons were found in
241 somatosensory and somatomotor areas, with additional neurons found at more anterior and

242 posterior locations (**Figure 5d**). No output projection patterns were identified within subregions of
243 the somatosensory and somatomotor areas (**Supplementary Figure 13**).

244 When converted to density, a different pattern of projection density became apparent
245 (**Figure 5e**). The highest densities of neurons were found in contralateral anterior and medial
246 neocortical regions, with peak regions exceeding 400 neurons per mm^3, more than twice the
247 highest density found in somatosensory and somatomotor regions. The most densely labeled
248 regions included infralimbic, orbital, and prelimbic areas but excluded the frontal pole (**Figure 5e**).

249 To build a single map from the results of many injections, we fitted a GLM to the data in
250 the same way as for thalamic labeling. Sensorimotor and frontal regions were strongly
251 represented in the model weights. The GLM also sharpened the cerebellocortical topographical
252 relationship (**Figure 5d**). All injected cerebellar sites showed high weighting in somatomotor and
253 somatosensory cortex. In addition, lobules I-V showed significant weights in anterior cingulate
254 cortex. Weak clusters of connectivity were also visible in visual and retrosplenial cortex. Mean
255 neuron density by primary injection site (**Figure 5g**) revealed that all injected cerebellar sites sent
256 dense projections to infralimbic cortex. Cerebellar vermis (lobules VI-X) and crus I sent denser
257 projections than other cerebellar injection sites to infralimbic, prelimbic, and orbital cortex (**Figure**
258 **5g**). A similar pattern was observed by taking the maximum of the fraction of neurons across each
259 cerebellar region, where the majority of neurons were found in the somatosensory and
260 somatomotor cortex and a smaller number of neurons were found the retrosplenial, agranular
261 insular, anterior cingulate, and orbital cortex (**Supplementary Figure 14**).

262 **Cerebellar paths reach reward-based structures in striatum and hypothalamus and project**
263 **modestly to ventral tegmental area**

264 Among other putative monosynaptic targets of the cerebellar nuclei, an area of renewed
265 focus has been the ventral tegmental area (VTA)[42,43], including a recent report of cerebellar

266 influence over reward processing[44]. We used our anterograde tracing pipeline to compare the
267 relative projection strengths of contralateral cerebellar paths to thalamus and two midbrain
268 dopaminergic areas, VTA and the substantia nigra (**Supplementary Figure 15**). We found that
269 the total number of neurons in contralateral VTA[45] was considerably lower than in thalamic
270 regions, consistent with known tracing[23,32,43,44]. Normalized to density per unit volume of the target
271 region, VTA projections were less than one-third as strong as projections to VPM, MD, and TRN.
272 Cell count densities in substantia nigra (SNr and SNc) were even lower than in VTA. In summary,
273 cerebellar projections to VTA constituted a moderate-strength projection, smaller in strength than
274 thalamic pathways but greater than other dopaminergic targets.

275 Like the VTA, striatal regions are also involved in reward learning. The cerebellar cortex
276 is known to project to basal ganglia trisynaptically via the cerebellar nuclei and thalamus[46]. Among
277 striatal regions, at our neocortical labeling timepoint we observed the most labeling in the caudate,
278 nucleus accumbens, and cortical amygdala. Labeling was dense in nucleus accumbens,
279 septohippocampal and septofimbrial nuclei as well as central/medial amygdala (**Supplementary**
280 **Figure 16**). At the thalamic and neocortical timepoints we also quantified hypothalamic
281 connectivity observing relatively strong expression in the lateral area as well as the periventricular
282 nucleus. We also observed high variability in projection density, likely related to the small volumes
283 of hypothalamic nuclei (**Supplementary Figure 17**). At both time points, we observed strong
284 labeling in the lateral hypothalamic area, which has been shown to regulate feeding and reward[47]
285 and the zona incerta, a well established recipient of DCN output[48].

286 **Cerebellum-neocortical paths strongly innervate deep neocortical layer neurons**

287 To investigate the layer-specific contributions of cerebellar paths to neocortex, we
288 examined laminar patterns of expression at the neocortical time point of H129-VC22 injections
289 (**Figure 6**). To minimize near-surface false positives, 60 μm was eroded from layer 1. In most

290 neocortical areas, the most and densest anterogradely labeled neurons were found in layers 5,
291 layers 6a and 6b (**Figure 6b,c**). No differences were found among the layer-specific patterns
292 resulting from injections to anterior vermis, posterior vermis, and posterior hemisphere ($p>0.95$,
293 ANOVA, two-tailed, 3 injection groups).

294 The layer-specificity of thalamocortical connections varies by neocortical region[49,50]. A
295 common motif of thalamocortical projections is strong innervation of layer 6 neurons, especially
296 in sensory regions[51,52]. In sensorimotor regions (somatomotor and somatosensory), over 40% of
297 our labeled cells were found in layer 6, a higher fraction than in other categories of neocortex
298 (**Figure 6b**). To validate these findings, we injected H129-VC22 at midline lobule VIa in Thy1-
299 YFP mice, which express YFP primarily in layer 5. These injections revealed viral labeling in
300 neocortex subjacent to YFP (**Supplementary Figure 18**).

301 Sensory regions are known to receive thalamic innervation of layer 4 neurons[51], However,
302 classical tracing typically does not identify the cellular target, only the cortical layer where the
303 synapse occurs[53]. We found that labeled layer 4 neurons comprised only 10% of cells in
304 somatosensory cortex and even less in other sensory regions (gustatory, visceral, temporal,
305 visual). Our results are consistent with the fact that thalamocortical synapses often occur in a
306 more superficial layer than the postsynaptic neuron[54].

307 A different pattern was seen in rhinal cortex, which forms part of the medial temporal
308 system for declarative memory. Rhinal regions (perirhinal, ectorhinal, and entorhinal) had the
309 highest fraction of layer 2/3 neurons (**Figure 6c,d,e**). This finding recalls the observation that in
310 associative neocortical regions, thalamocortical axons send substantial projections to superficial
311 layers[52]. Frontal and other association regions showed patterns that were intermediate between
312 sensorimotor and rhinal regions, while infralimbic, prelimbic, orbital, and anterior cingulate cortex
313 also received more and denser projections to layer 1 (**Figure 6c,d,e**). The share of labeling found
314 in in layer 5 and 6 neurons was higher for frontal nonmotor regions than for other cortical areas.

315 Taken together, our analysis reflects past findings that thalamic influences on neocortex arrive
316 first through superficial and deep layer pathways[54] (**Figure 6f**).

317 **Pseudorabies virus reveals strong descending somatomotor influence**

318 To characterize descending paths from neocortex to the cerebellum, we performed a
319 series of injections of pseudorabies virus Bartha strain (PRV-Bartha), a strain that travels entirely
320 in the retrograde direction (**Figure 7a,b,c**). In pilot experiments, expression was strong in
321 neocortex at 80 hpi. To isolate layer 5 neurons, whose axons comprise the descending
322 corticopontine pathway, we analyzed neurons registered to deep layers, which comprised 64% of
323 all contralaterally labeled neocortical neurons (**Supplementary Figure 19**).

324 Similar to the anterograde tracing results, we found the largest proportion of neurons in
325 somatosensory and somatomotor areas (**Figure 7d,f, Supplementary Figure 13**). Normalized to
326 volume, neuron densities were highest in somatosensory, somatomotor, and frontal cortex
327 (**Figure 7e,g**). Two regions identified as sources of corticopontine axons by classical tracing[55]
328 were labeled: anterior cingulate areas from injection of lobule VI and VII, and agranular insular
329 cortex from crus II. In addition, retrosplenial and auditory areas were labeled from injection of
330 paramedian lobule and copula pyramidis.

331 A GLM fitted to the data by the same procedure as the HSV-H129 tracing showed highest
332 weighting in somatomotor, somatosensory, and frontal regions (**Figure 7f**). Weights in
333 retrosplenial and visual cortex were smaller for vermal injections, and weights in gustatory,
334 agranular insula, and visceral cortex were elevated for simplex and crus II injections. Averaging
335 neuron density by primary injection site revealed all injected cerebellar sites received dense
336 projections from somatomotor and somatosensory cortex. Lobules I-VII and crus II received
337 denser projections from anterior cingulate and prelimbic cortex compared to other cerebellar

338 injection sites. Crus II also received dense projections from infralimbic, agranular insula,
339 gustatory, ectorhinal, and visceral cortex.

340 Descending corticopontine projections are known to be largely contralateral. To test the
341 extent to which descending paths remain contralateral across multiple synaptic steps, we
342 quantified the ratio of contralateral to ipsilateral cells for PRV-Bartha injections. Contralateral cells
343 outnumbered ipsilateral cells in all major neocortical areas, with average contralateral-to-
344 ipsilateral ratios of 1.4 in frontal cortex, 1.7 in posterior cortex, and 3.2 in somatomotor and
345 somatosensory cortex. Contralateral-to-ipsilateral ratios were higher for hemispheric injection
346 sites than vermal sites (**Supplementary Table 1**).

347 Ascending axonal projections of cerebellar nuclei are known to largely decussate to reach
348 contralateral midbrain structures[56]. For H129-VC22 injections, we observed bilaterality at both the
349 thalamic and neocortical timepoints. At the thalamic timepoint, the mean ratio of contralateral cells
350 to ipsilateral cells was 2.5 in sensorimotor nuclei and 1.0 in polymodal association nuclei.
351 Contralateral-to-ipsilateral ratios were highest for hemispheric injection sites (**Supplementary**
352 **Table 1**). Taken together, our HSV-H129 and PRV-Bartha observations suggest that the
353 organization of projections between cerebellum and neocortex is, by total proportion, to
354 sensorimotor cortical areas, most strongly contralateral in pathways that concern movement, and
355 more symmetrically distributed for nonmotor paths.

356 **c-Fos mapping reveals brainwide patterns of activation consistent with transsynaptic**
357 **tracing**

358 The reciprocal paths we have identified suggest that cerebellum incorporates descending
359 information and influences forebrain processing through diverse thalamocortical paths. To test
360 whether the functional strength of ascending paths was commensurate with their anatomical
361 connection, we measured expression of the immediate early gene c-Fos after optogenetic

362 perturbation of cerebellar activity (**Figure 8**). c-Fos expression reflects cumulative neural activity
363 and provides an independent means of quantifying long-distance influence. We expressed the
364 hyperpolarizing proton pump ArchT in Purkinje cells by injecting rAAV1-CAG-FLEX-ArchT-GFP
365 into the cerebellar vermis of L7-Cre+/- mice, using L7-Cre-/- mice as controls (**Figure 8a**).
366 Inactivation of Purkinje cells, which inhibit neurons of the cerebellar nuclei, would be expected to
367 have a net excitatory effect on thalamic and therefore neocortical activity.

368 Photostimulation led to reductions in Purkinje cell firing rate that were restricted to the
369 light-flash period and led to no perturbations in arm speed during treadmill running
370 (**Supplementary Figure 20**). After 1 hour photostimulation over lobule VI, either in mice
371 expressing ArchT (Cre+/-) or in nonexpressing controls (Cre-/-), brains were removed and cleared
372 using iDISCO+, then immunohistochemically stained for c-Fos using AlexaFluor-790 as the
373 fluorophore, and analyzed using ClearMap[22] (**Figure 8b,c**; **Supplementary Figure 21**) for
374 comparison with HSV-H129 tracing (**Figure 8d**).

375 Fourteen structures were identified having both significant count differences by a
376 nonparametric t-test and an activation ratio (defined as stimulation-group c-Fos average count
377 divided by control-group average) greater than 2.5 (**Figure 8e,f**). The strongest activation ratios
378 occurred in the anterior cingulate cortex, centrolateral nucleus of the thalamus, and the nucleus
379 accumbens (**Figure 8f**). Lobule VI itself also showed elevated c-Fos counts, as expected for
380 pulsed-light inactivation of Purkinje cells[57]. A voxel-wise t-test on cell count volumes
381 (**Supplementary Figure 22**) showed strong c-Fos expression in frontal neocortical regions,
382 especially in deep and middle neocortical layers. These findings are consistent with transsynaptic
383 tracing using both automated analysis of cleared tissue (**Supplementary Figure 19**) and standard
384 tissue sectioning and epifluorescent microscopy (**Supplementary Figure 18**).

385 Among neocortical regions, mean c-Fos stimulation-to-control cell density ratios and
386 H129-VC22 expression density was highly correlated (**Figure 8g**; c-Fos ratio vs. log HSV
387 expression r=+0.66, p=0.004), indicating that brainwide patterns of neural activity coincide with

388 patterns of ascending polysynaptic targets from lobule VI. Subcortical examination of c-Fos brains
389 revealed further broad similarities in expression with H129-VC22 labeling, including pontine
390 nuclei, midbrain, superior colliculi, and hypothalamus (**Supplementary Figure 23 and 24**).
391 Overall, these data show that c-Fos-based measures of brain activation coincide well with
392 patterns of anatomical projection as measured by transsynaptic viral labeling.

393 **DISCUSSION**

394 We found that ascending synaptic paths from the cerebellum can be classified into three
395 homologous systems serving sensorimotor, flexible cognitive, and modulatory functions (**Figure**
396 **9**). Parallel paths to several of these systems often originated from a single injection site. Well-
397 known sensorimotor regions contained the most connections by total proportion, but nonmotor
398 paths achieved comparable or higher local connection densities. Overall, these paths reached
399 nearly all parts of neocortex after passing through a variety of thalamic, striatal, and midbrain
400 structures.

401 In both neocortex and thalamus, the majority of total count of neurons labeled by
402 anterograde (HSV-H129) or retrograde (PRV-Bartha) viruses were found in structures classified
403 as sensorimotor, including ventral anterior-lateral (VAL; some portions termed ventrolateral (VL)
404 in older atlases[58]) and ventromedial (VM) thalamic nuclei[59]. By per-volume density of labeled
405 neurons, the strongest ascending projections went to anterior cingulate, prelimbic and infralimbic
406 cortex, as well as agranular and orbital areas. We also observed substantial relative labeling in
407 the VPM (sensorimotor), reticular thalamic (modulatory), and mediodorsal (associative) nuclei,
408 providing substrates for a variety of brain functions.

409 Although paths from cerebellum to thalamus and neocortex have been well-reported in
410 the past, differences from previous approaches may arise for several reasons. Traditional tracers
411 that do not cross synapses emphasize large presynaptic axons and extend only to their
412 terminations, which can be up to hundreds of microns away from postsynaptic neuronal cell

413 bodies. Such a distinction between axonal and transsynaptic tracing may account in part for the
414 strength of our observed projection to TRN neurons, which have elaborate dendritic processes
415 that extend into other thalamic nuclei[60]. Similarly, neocortical layer 5/6 pyramidal neuron dendrites
416 extend to superficial layers where thalamocortical synapses occur, and presynaptic fiber tracing
417 reveals connectivity to some superficial layers[53] while electrophysiological recordings identify
418 cortical recipient neurons in deeper layers[54]. Our neocortical labeling is consistent with
419 electrophysiological recordings.

420 A major architectural theme of cerebellar-neocortical interaction is that of closed loops, in
421 which it has been suggested that each region of neocortex may have a small number of principal
422 partners in the cerebellum, and vice versa[11]. Our work builds upon and broadens that picture.
423 Ascending cerebellar paths are influenced by a variety of both motor and nonmotor descending
424 information, thus forming a bidirectionally communicating loop between the neocortex and
425 cerebellum. Descending pathways from the neocortex were most strongly concentrated in
426 somatomotor and somatosensory cortex. Consistent with recent anterograde tracing from
427 neocortex to mossy fibers[61], by far the strongest neocortical paths to cerebellum originated from
428 somatosensory and somatomotor sites. Although that study did not encompass frontal nonmotor
429 neocortex, transsynaptic tracing in rat[15] does align with our observation of strong input from frontal
430 areas (prelimbic, infralimbic, insula and orbital cortices) to crus II. Taken together, connectivity
431 patterns observed suggest that the cerebellum receives information from a wide variety of
432 neocortical sites to exert returning influence on a similarly broad range of thalamic and neocortical
433 targets.

434 **Nonmotor functions of the cerebellum.** Among the cerebellar injection sites, nonmotor
435 functions have been suggested for lobule VI in the posterior vermis, and crus I and II in the
436 posterior parts of the hemispheres. We found that lobule VI sent strong projections to mediodorsal
437 and paraventricular nucleus of thalamus and to frontal neocortical regions, which serve a wide
438 range of cognitive and emotional functions[62,63]. Because the refinement of neural circuitry is

439 activity-dependent[64], this projection may also potentially account for the observation that
440 cerebellar perturbation of lobule VI can affect cognitive and social development in rodents[2] and
441 humans[6], and the association of posterior vermal abnormalities with a high risk of ASD[36].
442 Optogenetic stimulation of lobule VI also led to strong activation of c-Fos in the nucleus
443 accumbens (NAc), the main component of the ventral striatum, which is implicated in reward
444 learning and motivation[65]. This observation is consistent with our observation of NAc labeling at
445 the neocortical timepoint of HSV anterograde tracing (**Supplementary Figure 18**).

446 We found that crus I projects to lateral dorsal and paraventricular nuclei of the thalamus,
447 as well as frontal neocortical regions. Crus I has previously been observed to be activated during
448 working memory[66]. Novel projections from the DCN through lateral dorsal thalamus to regions
449 involved in working memory, the hippocampus and retrosplenial cortex, have been described
450 previously in the mouse[67]. In mice, disruptions of crus I activity in adulthood or juvenile life lead
451 to deficits in adult flexible behavior[2,68]; adult disruption shortens the time constant of a working
452 memory task[3]. Crus I also projects to paraventricular nucleus[62], which provides a possible
453 substrate for the observation that juvenile disruption of crus I leads to long-lasting deficits in social
454 preference[2]. In addition, we observed dense expression in septal and amygdalar regions
455 consistent with pathways established in rat and cat[69].

456 The cerebellum is known to be a site of sensory gating[70,71]. Tracing to thalamus suggests
457 that such gating might contribute to a broader regulatory network. Lobules (I-VII) and crus II sent
458 strong paths to thalamic reticular nucleus (TRN), a known monosynaptic target of the cerebellar
459 nuclei[72]. Our identification of neurons in the dentate and interpositus cerebellar nuclei that project
460 to TRN agrees with similar studies in rat[39,40] (**Supplementary Figure 12**) and cat[41].

461 TRN is the only thalamic nucleus that is inhibitory and the only one to send projections
462 exclusively within the thalamus itself. TRN may control sensory gain[73] and the flow of information
463 in and out of the neocortex[74]. TRN also receives a strong descending projection from neocortical
464 layer 6[74,75], a site of prominent expression in our work. This descending projection completes an

465 inhibitory loop, and has been suggested to contribute to neocortical oscillations and
466 synchrony[76,77]. Our findings add cerebellum as a substantial contributor to this modulatory
467 thalamocortical network.

468 **A pipeline for long-distance transsynaptic mapping.** Although many individual
469 projections within these pathways have been previously reported, our work presents a brainwide
470 survey of their relative strength. Polysynaptic transsynaptic tracing studies relied on time-
471 consuming human identification for analysis. More recently, tissue clearing has been used for
472 volumetric histological analyses, with the recent introduction of automated methods for cell
473 identification[22]. We find that cell counting can be efficient, accurate, and scalable to the whole
474 brain. Our mapping project relied on our BrainPipe pipeline, which combines transsynaptic
475 tracing, whole-brain clearing and microscopy, automated neuron counting, and atlas registration.
476 BrainPipe should be scalable for larger datasets as the resolution of light-sheet microscopy
477 improves. Adapting BrainPipe to other experimental studies requires only a different annotated
478 dataset to train a new convolutional neural network to identify objects of interest. Our pipeline can
479 run on high-performance computing clusters, allowing for faster turnaround of results than other
480 analysis pipelines, such as ClearMap[22].

481 In creating our light-sheet brain atlas, we overcame the general problem of creating a
482 reference atlas for a different imaging modality from the ABA. Our solution consisted of three
483 steps: (1) align individually imaged brains to a single experimental brain serving as the initial
484 template, (2) average the post-aligned brains to obtain a project-specific atlas for precise
485 automated registration, and (3) learn the transform between the project-specific atlas and the field
486 standard. Our basic software package (github.com/PrincetonUniversity/pytlas) is capable of
487 efficiently generating atlases for other imaging modalities as well.

488 We took two approaches to quantifying relative projection strength: fraction of total
489 expression for an entire parent structure (*e.g.* whole thalamus or neocortex) or density of cells
490 within a nucleus or region. Fraction of total expression allows for relative comparison of projection

491 strengths within a parent structure, conveying information about the distribution of influence. In
492 contrast, density takes the local target structure into account and provides information about the
493 concentrated influence on a particular recipient target. For example, although the great majority
494 of projections to neocortex are found in somatomotor and somatosensory cortices, the smaller
495 prefrontal areas receive a higher density of projections. This suggests cerebellum's capacity for
496 influence on prefrontal areas, while smaller in total terms, might still provide a means by which
497 cerebellar disruptions lead to deficits in nonmotor behavior[2,68].

498 Our HSV-based transsynaptic approach was designed to identify disynaptic paths from
499 cerebellar cortex to thalamus and trisynaptic paths to neocortex. Our control experiments using
500 shorter timepoints (28 and 36 hpi) and brainstem analysis at the disynaptic timepoint indicate that
501 retrograde transport was minimal. However, a variety of longer anterograde paths are possible.
502 The fastigial nuclei have bilateral efferents to the ipsilateral brachium conjunctivum (BC) and, via
503 the uncinate fasciculus to the contralateral BC[10,78] and the cerebellar nuclei project to
504 hindbrain/midbrain targets in addition to thalamus[10,79]. Tracing from neurons in the dentate
505 (lateral) nucleus has been shown to have axons crossing the thalamic midline terminating in the
506 ipsilateral VL[40,80] (current atlas definitions mostly of VA-L; **Supplementary Figure 12**). Indeed,
507 we observed contralateral crossing of axons after AAV injections in the fastigial nucleus
508 (**Supplementary Figure 9**). Over long distances, where transport time is increasingly dominated
509 by axon-associated transport mechanisms[81], HSV-H129 may follow such alternative paths, as
510 well as retrograde paths for incubations of 96 hours or longer. We therefore restricted our analysis
511 to contralateral projections and the shortest necessary incubation times, decreasing risk for
512 asynchronous or retrograde spread. The correlation of the resulting observed labeling with c-Fos
513 activation suggests that our observations reflect major routes by which the cerebellum influences
514 neocortical function.

515 Our cerebellum-to-thalamus projection data is broadly consistent with the literature,
516 though with more emphasis on sensory (*e.g.* VPM, DLG) over motor (*e.g.* VAL) structures. This

517 difference may arise from HSV-H129's ability to track the summed contributions of multiple
518 pathways with different intermediates. Convergent cerebellar projections to motor and sensory
519 neocortex have been recently characterized in the rat[19]. Some connectivity to sensory thalamus
520 may arise from vestibular nuclei[24,82,83]. Vestibular nuclei receive a well-known input from Purkinje
521 cells in flocculonodular cerebellum, but we found even more total input from other cerebellar
522 regions. In this way, cerebellar influence over a thalamic or neocortical target may be transmitted
523 via more than one path. Additional contrasts may arise from differences in the uptake, selectivity
524 and spread of tracers[84–86]. In particular, HSV spreads slower in large axons than small axons[87],
525 which may emphasize sensory pathways.

526 **From local cerebellar circuitry to global brain function.** The local circuitry of
527 cerebellum is thought to make rapid predictions about future states, which then modulate the
528 activity of other brain regions. In the motor domain, evidence suggests error learning through a
529 supervised learning process. Contextual information in this learning process comes from the
530 mossy fiber-granule cell pathway, and a teaching signal comes from the climbing fiber pathway.
531 This circuitry is homologous across cerebellar regions, with each part of the cerebellar cortex
532 managing a massive convergence of diverse incoming information from a distinct assortment of
533 distant brain regions. Initial fast and early learning occurs at parallel-fiber to Purkinje cell synapses
534 and other synapses[88]. Cerebellar and vestibular nuclei have their own information-processing and
535 learning rules and serve as an exit gateway to influence other brain regions[10,88]. The cerebellum
536 may generate predictions to fine-tune activity across nonmotor functions as well[3,6,89] as it is
537 composed of many modules, whose processing converges strongly onto cerebellar and vestibular
538 nuclei. Although classically these modules are considered to have specific extracerebellar
539 partners[13], our tracing quantifies the extent to which ascending cerebellar output paths from a
540 single site may provide the same predictive information to many targets with diverse functions at
541 the same time.

542 **METHODS**

543 **OVERVIEW OF AUTOMATED PIPELINE FOR TRANSSYNAPTIC TRACING**

544 In order to identify and quantify cerebellar connectivity on the long distance scale, we developed
545 a pipeline, BrainPipe, to enable automated detection of transsynaptically labeled neurons using
546 the mostly anterogradely-transported HSV-H129[26], identifying cerebellar output targets, and
547 retrogradely-transported PRV-Bartha[90], identifying the descending corticopontine pathway,
548 comprised mostly of layer 5 pyramidal neurons[91]. Mouse brains with cerebellar cortical injections
549 of Bartha or H129 were cleared using iDISCO+. We then imaged the brains using light-sheet
550 microscopy, generating brain volumes with a custom Python package. Next, to ensure accurate
551 anatomical identification across brains, we created a local light-sheet template, the Princeton
552 Mouse Brain Atlas (PMA) and quantified registration performance of individual volumes to the
553 local template. We then determined the transform between the PMA and the Allen Brain Atlas,
554 enabling standardization of our results with the current field standard. Next, to automatically and
555 accurately detect labeled cells, we developed a convolutional neural network whose performance
556 approached that of human classifiers.

557 **ANIMAL EXPERIMENTATION**

558 Experimental procedures were approved by the Institutional Animal Care and Use Committees of
559 Princeton University (protocol number 1943-19), the University of Idaho (protocol number 2017-
560 66), and the Dutch national experimental animal committees (DEC), and performed in accordance
561 with the animal welfare guidelines of the National Institutes of Health (USA) or the European
562 Communities Council Directive (Netherlands).

563 **VIRUS SOURCES**

564 HSV-1 strain H129 recombinant VC22 (H129-VC22) expresses EGFP-NLS, driven by the CMV
565 immediate-early promoter and terminated with the SV40 polyA sequence. To engineer this
566 recombinant, we used the procedure previously described to construct HSV-772, which
567 corresponds to H129 with CMV-EGFP-SV40pA[26]. We generated plasmid VC22 by inserting into
568 plasmid HSV-772 three tandem copies of the sequence for the c-Myc nuclear localization signal
569 (NLS) PAAKRVKLD[92], fused to the carboxy-terminus of EGFP. Plasmid VC22 contains two
570 flanking sequences, one of 1888-bp homologous to HSV-1 UL26/26.5, and one of 2078-bp
571 homologous to HSV-1 UL27, to allow insertion in the region between these genes. HSV-1 H129
572 nucleocapsid DNA was cotransfected with linearized plasmid VC22 using Lipofectamine 2000
573 over African green monkey kidney epithelial cell line Vero (ATCC cell line CCL-81), following the
574 manufacturer's protocol (Invitrogen). Viral plaques expressing EGFP-NLS were visualized and
575 selected under an epifluorescence microscope. PRV-152 (PRV Bartha[90]), which drives the
576 expression of GFP driven by the CMV immediate-early promoter and terminated with the SV40
577 polyA sequence, was a gift of the laboratory of Lynn W. Enquist. Adeno-associated virus was
578 obtained from Addgene (https://www.addgene.org).

579 **IN VIVO VIRUS INJECTIONS**

580 **Surgery for HSV and PRV injections.** Mice were injected intraperitoneally with 15% mannitol in
581 0.9% saline (M4125, Sigma-Aldrich, St. Louis, MO) approximately 30 minutes before surgery to
582 decrease surgical bleeding and facilitate viral uptake. Mice were then anesthetized with isoflurane
583 (5% induction, 1-2% isoflurane/oxygen maintenance vol/vol), eyes covered with ophthalmic
584 ointment (Puralube, Pharmaderm Florham Park, NJ), and stereotactically stabilized (Kopf Model
585 1900, David Kopf Instruments, Tujunga, CA). After shaving hair over the scalp, a midline incision
586 was made to expose the posterior skull. Posterior neck muscles attaching to the skull were

587 removed, and the brain was exposed by making a craniotomy using a 0.5 mm micro-drill burr
588 (Fine Science Tools, Foster City, CA). External cerebellar vasculature was used to identify
589 cerebellar lobule boundaries to determine nominal anatomical locations for injection. Injection
590 pipettes were pulled from soda lime glass (71900-10 Kimble, Vineland, NJ) on a P-97 puller
591 (Sutter Instruments, Novato, CA), beveled to 30 degrees with an approximate 10 μm tip width,
592 and backfilled with injection solution.

593 **AAV deep cerebellar nuclear injections.** During stereotaxic surgery, mice were anesthetized
594 with isoflurane (PCH, induction: 5%; maintenance: 2.0-2.5%) and received a mannitol injection
595 intraperitoneally (2.33 g/kg in milli-Q) and a Rimadyl injection subcutaneously (5 mg/kg Carprofen
596 50 mg/ml, Pfizer, Eurovet, in NaCl). Body temperature was kept constant at 37°C with a feedback
597 measurement system (DC Temperature Control System, FHC, Bowdoin, ME, VS). Mice were
598 placed into a stereotactic frame (Stoelting, Chicago laboratory supply), fixing the head with stub
599 ear bars and a tooth bar. DURATEARS® eye ointment (Alcon) was used to prevent corneal
600 dehydration. A 2 cm sagittal scalp incision was made, after which the exposed skull was cleaned
601 with sterile saline. Mice were given 2 small (Ø±1 mm) craniotomies in the interparietal bone (-2
602 mm AP relative to lambda; 1.8 mm ML) for virus injection. Craniotomies were performed using a
603 hand drill (Marathon N7 Dental Micro Motor). A bilateral injection of AAV5-Syn-ChR2-eYFP (125
604 nl per hemisphere, infusion speed ~0.05 μl/minute) in the AIN was done using a glass micropipette
605 controlled by a syringe. This AAV was used because it gave reliable strong axon terminal labeling
606 and because the animals were also used for another optogenetic study. After slowly lowering the
607 micropipette to the target site (2.2 mm ventral), the micropipette remained stationary for 5 minutes
608 before the start of the injection, and again after finishing the injection. Micropipette was then
609 withdrawn slowly from the brain (ejection speed ~1 mm/minute). Craniotomies and skin were
610 closed and mice received post-op Rimadyl. Animals were perfused transcardially 3 weeks after
611 viral injection using 4% PFA. Brains were collected post mortem, stained for co-stained for DAPI

612 (0100-20, Southern Biotech, Birmingham AL), coronally sectioned at 40 µm/slice and imaged with
613 an epifluorescent microscope at 20x (Nanozoomer, Hamamatsu, Shizuoka, Japan).

614 **AAV TRN injections.** During stereotaxic surgery, mice (1-3 months of age) were anesthetized
615 with isoflurane (VetOne, induction: 3-5%; maintenance: 1.5-2.5%). For analgesic support mice
616 provided oral carprofen *ad libitum* from the day before and through 24hrs after surgery and given
617 slow release meloxicam (4mg/kg; ZooPharm, Larami, WY). Body temperature was maintained by
618 a warming blanket (Stoelting, Wood Dale, IL) under the animal throughout the surgery. Mice were
619 placed into a stereotactic frame (Kopf, Tujunga, CA), fixing the head with non-rupture ear bars, a
620 tooth bar and nose cone. Puralube® Vet eye ointment (Dechra) was used to prevent corneal
621 dehydration. A sagittal scalp incision was made, after which the exposed skull was cleaned with
622 sterile saline. A single small craniotomy (Ø0.6 mm) was made in the parietal bone (−1.3 mm AP
623 relative to lambda; 2.3 mm to the right of ML) for virus injection. Craniotomies were performed
624 using a stereotaxic-mounted drill (Foredom K.1070 Micromotor Drill). A unilateral 200-300 nl
625 injection of AAVrg-hSyn-Chronos-GFP ($9.0x10^{12}$; Addgene, Watertown, MA) at an infusion speed
626 of 0.01 µl/minute in the right TRN was done using a glass syringe and needle (Hamilton Company,
627 Franklin, MA). After slowly lowering the needle to the target site (-2.9 mm ventral), the needle
628 remained stationary for 1 minute before the start of the injection, and for 5 min after finishing the
629 injection. The needle was then withdrawn slowly from the brain. Craniotomies and skin were
630 closed using removable staples and mice continued to receive oral carprofen *ad libitum* for 24hrs
631 post-surgery. Animals were euthanized 20-25 days after viral injection and brains were fixed in
632 4% PFA. Brains were collected, frozen and coronally sectioned into 40 µm slices, then co-stained
633 with Hoechst 33324 (5 µg/ml; Invitrogen), chicken anti-GFP (1:500; Novus Biologicals; NB100-
634 1614), and rabbit anti-parvalbumin (1:500; ZRB1218; Millipore Sigma), and imaged with a
635 confocal fluorescence microscope at 10X and 20x (Nikon Instruments TiE Inverted Microscope

636 with Yokogawa X1 Spinning Disk) or epifluorescence microscope at 2.5X and 10X (Zeiss Axio
637 Imager.M2).

638 **Transsynaptic viral tracing for tissue clearing (HSV-H129 and PRV-Bartha).** Transsynaptic
639 viral tracing studies used male and female 8-12 week-old C57BL/6J mice (The Jackson
640 Laboratory, Bar Harbor, Maine). Injection solution was prepared by making a 9:1 dilution of virus
641 stock to 0.5% cholera toxin B conjugated to Alexa Fluor 555 in saline (CTB-555, C22843, Sigma-
642 Aldrich; as per Ref. 93). At the timepoints used CTB-555 persisted at the injection site. Pipettes
643 were inserted perpendicular to tissue surface to a depth of approximately 200 μm. **Table 4**
644 describes injection parameters for each type of experiment.

645 Pressure injections delivered 80 to 240 nl into the target location. Consistent with prior
646 literature we observed that minimum injections of 10^4 PFUs were required for successful HSV-
647 H129 infection[94]. This viral feature dictated a lower injection size limit. Smaller injections
648 consistently produced unsuccessful primary infections and thus no transsynaptic spread.
649 Unfortunately, this feature also prevented consistent injections of single zones as defined by
650 zebrin staining.

651 After viral injection, Rimadyl (0.2 ml, 50 mg/ml, Carprofen, Zoetis, Florham Park, NJ) was
652 delivered subcutaneously. At the end of the post-injection incubation period, animals were
653 overdosed by intraperitoneal injection of ketamine/xylazine (ketamine: 400 mg/kg, Zetamine, Vet
654 One, ANADA #200-055; xylazine: 50 mg/kg, AnaSed Injection Xylazine, Akorn, NADA #139-236)
655 and transcardially perfused with 10 ml of 0.1 M phosphate buffer saline (PBS) followed by 25 ml
656 10% formalin (Fisher Scientific 23-245685). Tissue was fixed overnight in 10% formalin before
657 the iDISCO+ clearing protocol began.

658 For anterograde transport experiments, incubation times were determined by
659 immunostaining for viral antigens at various timepoints (30, 36, 41, 49, 54, 58, 67, 73, 80, 82 and
660 89 hours post-injection) the canonical ascending pathway of cerebellar cortex to cerebellar nuclei

661 to thalamus to neocortex. For retrograde transport experiments, incubation times were
662 determined by immunostaining for GFP (48, 60, 72, 78, 81, 84 and 91 hpi) targeting the canonical
663 descending pathway: neocortex to brainstem to cerebellar cortex. We selected timepoints with
664 the goal of achieving sufficient labeling for detection, while minimizing incubation periods, given
665 that with increasing long distance, transport time is increasingly dominated by axon-associated
666 transport mechanisms[81,95–97], leading to labeling of alternative paths and retrograde paths after
667 96 hours[26]. Our selected timepoints were shorter than published timepoints (**Table 6**), and were
668 therefore likely to reduce the degree of supernumerary synaptic spread.

669 **Considerations when using transsynaptic tracing viruses**. For practical use in tracing,
670 transsynaptic viral tracers typically require doses close to the infectivity threshold. For H129, the
671 minimum dose is 10^4 pfus[94]; consistent with our injections). Although injecting close to the
672 infectivity threshold results in greater infection variability as well as failure to label all second- and
673 third- order neurons, it ensures the most specific transport, protecting against nonspecific
674 nontransneural transport[98,99].

675 To quantify possible retrograde HSV-H129 transport from the injection site[27]
676 (**Supplementary Figure 1**), we compared retrograde:anterograde density ratios for HSV-H129
677 and PRV at disynaptic (HSV-H129 54 hpi; PRV 80 hpi) timepoints. We used the dorsal column
678 nuclei, disynaptically retrograde from cerebellar cortex that lacks anterograde projections from
679 DCN, for retrograde spread. We used the DCN, monosynaptic anterograde, for anterograde
680 spread. PRV provides the maximum amount of retrograde labeling.

681 To minimize unintended further downstream synaptic spread, we performed empirical time
682 series and selected the minimal time that provided sufficient spread. We compared our time points
683 with known literature and found that we never exceeded published timepoints and often had
684 considerably shorter timepoints than other work (**Table 6**). Transsynaptic tracing is always at risk
685 for loss of synchrony with viral particles traveling along parallel polysynaptic circuits. For example,

686 the HSV-H129 neocortical timepoint will not be 100% thalamocortical target neurons, but may
687 contain a small fraction of “leading-edge” cells that are one step further. However, our shorter-
688 than-published timepoints suggests our studies minimize this risk. This also suggests that tissue
689 clearing is likely a more sensitive method, allowing for unbiased whole-brain observation of viral
690 spread. Previous studies, by nature of manual annotation, could only observe a small subset of
691 brain regions without robust quantification. Every tool, viral or nonviral, has its own differential
692 selectivity for different types of neurons; Alphaherpesviruses (such as PRV and HSV) have been
693 shown to spread faster in sensory peripheral nerves than motor paths[87,100]. Other viral tropism
694 differences have been directly studied in Rabies versus AAV[84] as well as tropism across AAV
695 serotypes[85,86]. Although HSV-H129 has its limitations with different spread characteristics across
696 strains[101] is it the most robust tool currently available for anterograde transsynaptic viral tracing.
697 Therefore likely some of differences between our findings and classically established literature
698 could be related to both the use of transsynaptic viruses as well as whole-brain statistical unbiased
699 quantification.

700 **VIRAL TRACING WITH TISSUE SECTIONING AND SLIDE-BASED MICROSCOPY**

701 **Viral tracing with classical sectioning-based histology: HSV-772 cerebellar injections.**
702 Adult Thy1-YFP male mice (YFP +, n=2, B6.Cg-Tg (Thy1-YFP)HJrs/J, 003782, The Jackson
703 Laboratory, 22 weeks), were prepared for surgery, in a similar fashion as in *Transsynaptic viral*
704 *tracing for tissue clearing (H129 and Bartha)*. We used the HSV recombinant HSV-772 (CMV-
705 EGFP, 9.02 x 10^8 PFU/ml; as in Ref. 26), a H129 recombinant that produces a diffusible EGFP
706 reporter. Again, using a 9:1 HSV:CTB-555 injection solution, 350 nl/injection was pressure
707 injected into two mediolateral spots in lobule VIa. Eighty hours post-injection, animals were
708 overdosed using a ketamine/xylazine mixture as described previously. Brains were extracted and
709 fixed overnight in 10% formalin and cut at 50 μm thickness in PBS using a vibratome (VT1000S,

710 Leica). Sections were immunohistochemically blocked by incubating for 1 hour in 10% goat serum
711 (G6767-100ML, Sigma-Aldrich, St. Louis, MO), 0.5% Triton X100 (T8787-50ML, Sigma-Aldrich)
712 in PBS. Next sections were put in primary antibody solution (1:750 Dako Anti-HSV in 2% goat
713 serum, 0.4% Triton X100 in PBS) for 72 hours at 4°C in the dark. Sections were washed in PBS
714 4 times for 10 minutes each, and then incubated with secondary antibody (1:300 Goat anti-rabbit-
715 AF647 in 2% goat serum, 0.4% Triton X100 in PBS) for two hours. Another series of PBS washes
716 (four times, 10 minutes each) before mounting onto glass microscope slides with a Vectashield
717 mounting agent (H-1000, Vector Laboratories, Burlingame, CA). Sections were fluorescently
718 imaged at 20x (Nanozoomer, Hamamatsu, Shizuoka, Japan) and at 63x with 5 μm z steps (Leica
719 SP8 confocal laser-scanning microscope).

720 **TISSUE CLEARING AND LIGHT-SHEET MICROSCOPY**

721 **iDISCO+ tissue clearing.** After extraction, brains were immersed overnight in 10% formalin. An
722 iDISCO+ tissue clearing protocol[22] was used (*Supplemental clearing worksheet*). Brains were
723 dehydrated step-wise in increasing concentrations of methanol (Carolina Biological Supply,
724 874195; 20, 40, 60, 80, 100% in doubly distilled H20 (ddH20), 1 hr each), bleached in 5%
725 hydrogen peroxide/methanol solution (Sigma, H1009-100ML) overnight, and serially rehydrated
726 (methanol: ddH20 100, 80, 60, 40, 20%, 1 hr each). Brains were washed in 0.2% Triton X-100
727 (Sigma, T8787-50ML) in PBS, then in 20% DMSO (Fisher Scientific D128-1) + 0.3 M glycine
728 (Sigma 410225-50G) + 0.2% Triton X-100/PBS at 37°C for 2 days. Brains were then immersed in
729 a blocking solution of 10% DMSO + 6% donkey serum (EMD Millipore S30-100ml) + 0.2% Triton
730 X-100 + PBS at 37°C for 2-3 days to reduce non-specific antibody binding. Brains were then twice
731 washed for 1 hr/wash in PBS + 0.2% Tween-20 (Sigma P9416-50ML) + 10 μg/ml heparin (Sigma
732 H3149-100KU) (PTwH).

733 For HSV and c-Fos antibody labeling, brains were incubated with primary antibody
734 solution (see **Table 4** for antibody concentrations) consisting of 5% DMSO + 3% donkey serum
735 + PTwH at 37°C for 7 days. Brains were then washed in PTwH at least 5 times (wash intervals:
736 10 min, 15, 30, 1 hr, 2 hr), immunostained with secondary antibody in 3% donkey serum/PTwH
737 at 37°C for 7 days, and washed again in PTwH at least 5 times (wash intervals: 10 min, 15, 30, 1
738 hr, 2 hr). Finally, brains were serially dehydrated (methanol: ddH20: 100, 80, 60, 40, 20%, 1 hr
739 each), treated with 2:1 dichloromethane (DCM; Sigma, 270997-2L):methanol and then 100%
740 DCM, and placed in the refractive index matching solution dibenzyl ether (DBE; Sigma, 108014-
741 1KG) for storage at room temperature before imaging.

742 **Light-sheet microscopy for transsynaptic tracing.** Cleared brain samples were glued (Loctite,
743 234796) ventral side down on a custom-designed 3D-printed holder and imaged in an index-
744 matched solution, DBE, using a light-sheet microscope (Ultramicroscope II, LaVision Biotec.,
745 Bielefeld, Germany). Version 5.1.347 of the ImSpector Microscope controller software was used.
746 An autofluorescent channel for registration purposes was acquired using 488 nm laser diode
747 excitation and 525 nm emission (FF01-525/39-25, Semrock, Rochester, New York). Injection
748 sites, identified by CTB-555, were acquired at 561 nm excitation and 609 nm emission (FF01-
749 609/54-25, Semrock). Cellular imaging of virally infected cells (anti-HSV Dako B011402-2) was
750 acquired using 640 nm excitation and 680 nm emission (FF01-680/42-25, Semrock). Cellular-
751 resolution imaging was done at 1.63 µm/pixel (1x magnification, 4x objective, 0.28 NA, 5.6 - 6.0
752 mm working distance, 3.5 mm x 4.1 mm field of view, LVMI-FLuor 4x, LaVision Biotech) with 3x3
753 tiling (with typically 10% overlap) per horizontal plane. Separate left- and right-sided illumination
754 images were taken every 7.5 micrometers step size using a 0.008 excitation-sheet NA. A
755 computational stitching approach[102] was performed independently for left- and right-side
756 illuminated volumes, followed by midline sigmoidal-blending of the two volumes to reduce
757 movement and image artifacts.

REGISTRATION AND ATLAS PREPARATION

Image registration. Most registration software cannot compute transformation with full-sized light-sheet volumes in the 100-200 gigabyte range due to computational limits. Using mid-range computers, reasonable processing times are obtained with file sizes of 300-750 megabytes, which for mouse brain corresponds to 20 μm/voxel. Empirically, we found that light-sheet brain volumes to be aligned ("moving") resampled to approximately 140% the size of the reference ("fixed") atlas volume yielded the best registration performance. Alignment was done by applying an affine transformations allowing for translation, rotation, shearing and scaling to generally align with the atlas, followed by b-spline transformation to account for brain-subregion variability among individual brains.

For uniformity among samples, registration was done using the autofluorescence channel, which has substantial autofluorescence at shorter wavelengths useful for registration[103]. In addition to autofluorescence-to-atlas registration, the signal channel was registered using an affine transformation to the autofluorescence channel to control for minor brain movement during acquisition, wavelength-dependent aberrations, and differences in imaging parameters[22].

Affine and b-spline transformations were computed using elastix[104,105]; see supplemental Elastix affine and b-spline parameters used for light-sheet volume registration. Briefly, the elastix affine transform allows for translation (t), rotation (R), shearing (G), and scaling (S) and is defined as:

$$\boldsymbol{T_\mu}(\boldsymbol{x}) = \boldsymbol{RGS}(\boldsymbol{x} - \boldsymbol{c}) + \boldsymbol{t} + \boldsymbol{c}$$

where c is a center of rotation and t is a translation. The elastix b-spline transformation allows for nonlinearities and is defined as:

$$\boldsymbol{T_\mu}(\boldsymbol{x}) = \boldsymbol{x} + \sum_{\boldsymbol{x}_k \in \mathcal{N}_{\boldsymbol{x}}} \boldsymbol{p}_k \boldsymbol{\beta}^3 \left(\frac{\boldsymbol{x} - \boldsymbol{x}_k}{\boldsymbol{\sigma}} \right)$$

781 Where x_κ are control points, β^3 (x) the B-spline polynomial, p_κ the b-spline coefficient vectors, Nx,
782 B-spline compact support control points, and σ is the b-spline compact control point-spacing (see
783 Ref. 106, pages 8-10 for reference). For the assignment of cell centers to anatomical locations,
784 we calculated transformations from cell signal space to autofluorescent space (affine only) and
785 autofluorescent space to atlas space (affine and b-spline; **Supplementary Figure 25**).

786 **Princeton Mouse Atlas generation.** To generate a light-sheet atlas with a complete posterior
787 cerebellum, autofluorescent light-sheet volumes from 110 mice (curated to eliminate distortions
788 related to damage, clearing, or imaging) were resampled to an isotropic 20 μm per voxel
789 resolution (**Figure 2** and **Supplementary Figure 3a**). We selected a single brain volume to use
790 as the fixed (template) volume for registration of the other 109 brains and computed the
791 transformations between the other 109 brains and the template brain. The registration task was
792 parallelized from ClearMap[22] adapting code for use on a Slurm-based[107] computing cluster.
793 After registration, all brains were pooled into a four-dimensional volume (brain, x, y, z),
794 and the median voxel value at each xyz location was used to generate a single median three-
795 dimensional volume. Flocculi and paraflocculi, which can become damaged or deformed during
796 extraction and clearing, were imaged separately from a subset of 26 brains in which these
797 structures were intact and undeformed. Manual voxel curation sharpened brain-edges in areas
798 where pixel intensity gradually faded. Finally, contrast limited adaptive histogram equalization
799 (skimage.exposure.equalize_adapthist) applied to the resulting volume increased local contrast
800 within brain structures, generating the final PMA (**Supplementary Figure 3b** and **Supplementary**
801 **Figure 26**). We then determined the transformation between the PMA and the Allen Brain
802 CCFv3[108] space in order to maintain translatability. Our software for basic atlas creation with an
803 accompanying Jupyter tutorial notebook is available online via
804 github.com/PrincetonUniversity/pytlas. Volumetric projection renderings were made using

805 ImageJ[109]; 3D project function (**Supplementary Figure 3a**). The PMA interactive three-
806 dimensional rendering of the PMA is available http://brainmaps.princeton.edu/pma_neuroglancer
807 and can be downloaded from https://brainmaps.princeton.edu/pma_landing_page.

808 **Statistical analysis of registration precision**. Precision of registration was measured by
809 quantifying euclidean landmark distances, defined by blinded users (similar to Ref. 110) between
810 the PMA and brains at different stages of registration. Estimated standard deviations are defined
811 as the median absolute deviation (MAD) divided by 0.6745. MADs were calculated with
812 Statsmodels[111] 0.9.0 (statsmodels.robust.mad). One measurement was considered to be user
813 error and was dropped in the theoretical-limit measurements, as it was over 12 times the median
814 of the other measures.

815 **Generation of 3D printable files.** To generate 3D printable Princeton Mouse Atlas files usable
816 for experimental and educational purposes, we loaded volumetric tiff files as surface objects using
817 the ImageJ-based 3D viewer. After resampling by a factor of 2 and intensity thresholding, data
818 were then imported to Blender[112], where surfaces were smoothed (Smooth Vertex tool) before
819 finally exporting as stereolithography (stl) files.

820 **AUTOMATED DETECTION OF VIRALLY LABELED CELLS**

821 **BrainPipe, an automated transsynaptic tracing and labeling analysis pipeline.** Whole-brain
822 light-sheet volumes were analyzed using a new pipeline, BrainPipe. BrainPipe consists of three
823 steps: cell detection, registration to a common atlas, and injection site recovery. For maximum
824 detection accuracy, cell detection was performed on unregistered image volumes, and the
825 detected cells were then transformed to atlas coordinates.

826 Before analysis, datasets were manually curated by stringent quality control standards.
827 Each brain was screened for (1) clearing quality, (2) significant tissue deformation from extraction
828 process, (3) viral spread from injection site, (4) antibody penetration, (5) blending artifacts related
829 to microscope misalignment, (6) injection site within target location, (7) successful registration,
830 and (8) CNN overlay of detected cells with brain volume in signal channel. Because of the
831 relatively high concentration of antibody solution needed for brain-wide immunohistochemical
832 staining, non-specific fluorescence was apparent at the edges of tissue, *i.e.* outside of the brain
833 and ventricles, in the form of punctate labeling not of cell origin. We computationally removed a
834 border at the brain edge at the ventricles to remove false positives, at the cost of loss of some
835 true positives (skimage.morphology.binary_erosion, **Table 4**). For neocortical layer studies, a
836 subregion of the primary somatosensory area: "primary somatosensory area, unassigned" in PMA
837 did not have layer-specific mapping in Allen Atlas space and was removed from consideration.

838 **Injection site recovery and cell detection.** Injection sites were identified in H129 studies by co-
839 injecting CTB with virus (**Supplementary Figure 27**) and in c-Fos studies using ArchT-GFP
840 expression. Post-registered light-sheet volumes of the injection channel were segmented to
841 obtain voxel-by-voxel injection-site reconstructions. Volumes were Gaussian blurred (3 voxels).
842 All voxels below 3 standard deviations above the mean were removed. The single largest
843 connected component was considered the injection site (scipy.ndimage.label, SciPy 1.1.0[113]).
844 CTB was selected for injection site labelling for transsynaptic tracing as it does not affect the
845 spread of alpha-herpesviruses and its greater diffusion due to its smaller size overestimates the
846 viral injection size by as much as two-fold[114,115]. Although typically used as a tracer itself, used
847 during the small window of ~80 hours post-injection, it did not have time to spread.
848 **Supplementary Figure 7** shows the percentage of cerebellum covered by at least one injection
849 in each of the three datasets. Lobules I-III, flocculus, and paraflocculus were not targeted.

850 **Automated detection of transsynaptically labeled neurons.**

851 To optimize cell detection for scalability, whole-brain light-sheet volumes (typically 100-150 GB
852 16-bit volumes) were chunked into approximately 80 compressed 32-bit TIF volumes per brain,
853 with an overlap of 192 x 192 x 20 voxels in xyz between each volume, and stored on a file server.
854 For deploying the custom-trained cell-detection neural network, the file server streamed
855 the volumes to a GPU cluster for segmentation. Once the segmentation was completed, the soma
856 labels were reconstructed across the entire brain volume from the segmented image on a CPU
857 cluster by calculating the maximum between the overlapping segments of each volume. The
858 reconstructed brain volumes after segmentation were stored as memory-mapped arrays on a file
859 server. Coordinates of cell centers from the reconstructed volumes were obtained by thresholding,
860 using the established threshold from training evaluation, and connected-component analysis.
861 Additionally, measures of detected cell perimeter, sphericity, and number of voxels it spans in the
862 z-dimension were calculated by connected-component analysis for further cell classification if
863 needed. The final output consisted of a comma-separated values file that includes the xyz
864 coordinates as well as measures of perimeter, sphericity, and number of voxels in the z-dimension
865 for each detected cell in the brain volume.

866 **Convolutional neural network training**. Supervised learning using CNN is useful in complex
867 classification tasks when a sufficient amount of training data is available. Annotated training
868 volumes were generated by selecting volumes at least 200 x 200 x 50 pixels (XYZ) from full-sized
869 cell channel volumes. To ensure training data were representative of the animal variability across
870 the whole-brain, training volumes were selected from different anatomical regions in different
871 brains with various amounts of labeling (**Table 2** for dataset description). Annotations were
872 recorded by marking cell centers using ImageJ[109]. To generate labeled volumes, Otsu's
873 thresholding method (skimage.filters.threshold_otsu, Scikit-Image[116] 0.13.1) was applied within
874 windows (30 x 30 x 8 voxels, XYZ) around each center to label soma. Using annotated volumes,

875 we trained a three-dimensional CNN with a U-Net architecture[117,118]
876 (github.com/PrincetonUniversity/BrainPipe). A 192 x 192 x 20 CNN window size with 0.75 strides
877 was selected. The training dataset was split into a 70% training, 20% validation, and 10% testing
878 subset. Training occurred on a SLURM-based GPU cluster. During training, the CNN was
879 presented with data from the training dataset, and after each iteration its performance was
880 evaluated using the validation dataset. Loss values, which measure learning by the CNN,
881 stabilized at 295,000 training iterations, at which point training was stopped and the CNN was
882 evaluated for performance, as a risk in machine learning is overfitting, *i.e.* the possibility that the
883 neural network will learn particular training examples rather than learning the category.

884 **Evaluation of CNN.** To determine CNN performance on H129 data, we calculated an F1 score
885 (Ref. 119). First, we needed to compare CNN output with our ground truth annotations by
886 quantifying true positives (TP), false negatives (FN), and false positives (FP). We defined human-
887 annotation as ground truth, consistent with the machine learning field[120]. Our neural network
888 architecture produced a voxel-wise 0 (background) to 1 (cell) probability output. To determine a
889 threshold value for binarization of the continuous 0-1 CNN-output values, F1 scores as a function
890 of thresholds between 0 and 1 were determined (**FIgure 1f**). Connected-component analysis
891 (scipy.ndimage.label) grouped islands of nonzero voxels to identify each island as a putative cell.
892 Pairwise Euclidean distances (scipy.spatial.distance.euclidean) were calculated between CNN-
893 predicted cell centers and human-annotated ground truth centers. Bipartite matching serially
894 paired closest predicted and ground truth centers, removing each from unpaired pools.
895 Unmatched predicted or ground truth centers were considered FPs or FNs, respectively.
896 Prediction-ground truth center pairs with a Euclidean distance greater than 30 voxels (~49 μm)
897 were likely inaccurate and not paired.

898 The F1 score was defined as the harmonic average of precision and recall. Precision is
899 the number of correct positive results divided by the number of all positive results returned by the

classifier, *i.e.* TP/ (TP+FP). Recall is the number of correct positive results divided by the number of all samples that should have been identified as positive, *i.e.* TP/ (TP+FN). The F1 score reaches its best value at 1 (perfect precision and recall) and worst at 0. Using a 20 voxel cutoff instead of 30 gave 0.849 and 0.875 for human-CNN and human-human F1 scores, respectively. To determine CNN performance metrics, the testing dataset, which the network had yet to be exposed to was finally run using the established threshold producing an F1 score of 0.864. To generate the precision-recall curve, precision and recall values were calculated between thresholds of 0.002 and 0.998 with a step size of 0.002. Values of precision and 1-recall were used to plot the curve. The area-under-curve of the precision-recall curve was calculated using the composite trapezoidal rule (numpy.trapz).

Statistical analysis of transsynaptic tracing data. For initial inspection of thalamic or neocortical neurons, each injected brain was sorted by cerebellar region with the greatest volume fraction of the injection (as in Ref. 2; this region was defined as the primary injection site. Injections from each "primary" region were then pooled and averaged per thalamic nucleus (**Figure 3f**).

Two primary methods of quantification were used, fraction of all labeled neurons in the thalamus or neocortex, and density within particular structures. Fraction of neurons is defined as the total labelled neuron count within a structure (*e.g.* VAL) divided by the main parent structure (*e.g.* thalamus). This number is useful as it gives relative target projection strength relative to other projection strengths within the parent structure. However, this does not provide information in non-relative terms. Density, defined as total labelled neurons divided by volume of the structure, takes into account the relative sizes for each structure, allowing for more absolute comparisons of recipient structures. In anterograde examples, density therefore provides information on the concentration of influence a cerebellar region may have on a target structure.

923 **Generalized linear model analysis.** Contribution of each cerebellar meta-lobule to viral spread
924 in each neocortical or thalamic region was fitted to a generalized linear model (GLM) consisting
925 of an inhomogeneous Poisson process as a function of seven targeted cerebellar regions ("meta-
926 lobules"). The predictor variables were x_j, where $x_j$is defined as the fraction of the total injection
927 to be found in the j-th meta-lobule, such that $\Sigma\, x_j = 1$. The outputs to be predicted were y_k defined
928 as the fraction of the total number of cells in the entire neocortex (or thalamus) to be found in the
929 k-th region. For the resulting fit coefficients β_{jk}, the change in $\hat{y}_k$ arising from a unit change in x_j
930 is $e^{\beta_{jk}} - 1$. In **figures 4f**, **6f,** and **8f,** the heatmap indicates a measure of confidence, defined as
931 the coefficient (β_{jk}) divided by the coefficient's standard error.
932 To determine greater than chance significant weights, we compared significant weights
933 computed from the t-stats of the coefficients with those observed in a shuffle-based null model in
934 which predictors were shuffled uniformly at random (n = 1,000). We found that the true number
935 of positive significant weights is significantly greater than that expected under the null model with
936 a one-sided, non-parametric $p < 0.05$. In **Figure 7**, the neocortical region "Frontal pole, cerebral
937 cortex" was excluded from generalized linear model analysis due to zero counts across all brains
938 for the region.

939 **IMMUNOFLUORESCENCE IMAGE AND ANALYSIS**

940 **AAV DCN Injections.** To visualize YFP labeled fibers and vGluT2-positive terminals in the
941 thalamus, 40 micron thick slices were stained for vGluT2 anti-guinea pig Cy5 (Millipore Bioscience
942 Research reagent 1:2000 diluted in PBS containing 2% NHS and 0.4% Triton). Images were taken
943 using a confocal LSM 700 microscope (Carl Zeiss). Terminals positive to VGluT2 staining were
944 identified and morphologically studied using confocal images that were captured using the
945 following excitation wavelengths: 488 nm (YFP) and 639 nm (Cy5). High resolution image stacks

946 were acquired using a 63X1.4 NA oil objective with 1X digital zoom, a pinhole of 1 Airy unit and
947 significant oversampling for deconvolution (voxel dimension is: 46 nm width x 46 nm length x 130
948 nm depth calculated according to Nyquist factor; 8-bit per channel; image plane 2048 x 2048
949 pixels). Signal-to-noise ratio was improved by 2 times line averaging. Image stacks were
950 deconvolved using Huygens software (Scientific Volume Imaging). With a custom-written Fiji-
951 scripts (ImageJ) we identified putative synaptic contacts, *i.e.* YFP-positive varicosities that
952 colocalized with vGluT2-staining, following the same analysis pipeline as Ref. 59 (script available
953 upon reasonable request). The color channels (YFP and Cy5) of the images were split to get
954 separate stacks. The YFP and Cy5 channels were Gaussian blurred (sigma = 1) and selected by
955 a manually set threshold. A binary open function was done on both images (iterations = 4, count
956 = 2) and objects were removed if their size was <400 pixels (YFP). A small dilatation was done
957 on the red image (iteration = 1, count = 1). With the image calculator an 'and-operation' was done
958 using the binary red and green image. The values 255 (white) of the binary YFP image were set
959 to 127. This image and the result of the AND-operation were combined by an OR-operation. The
960 resulting image was measured with the 3D-object counter plugin for volumes and maximum
961 intensities. Only objects containing pixels with an intensity of 255 (overlap) are taken in account
962 for particle analysis. Estimation of synapse density (number of terminals/area μm^3) was obtained
963 for each image by dividing the number of terminals by the image area[121]. Regression between
964 AAV and HSV-H129 density was performed using two-sided Pearson's regression was performed
965 (R, cor.test).

966 **C-FOS MAPPING EXPERIMENT**

967 **c-Fos mapping after optogenetic perturbation.** Neural activity has been shown to increase c-
968 Fos, an immediate-early gene product[122]. Mapping of c-Fos expression used L7-Cre +/- (n=10)
969 and -/- (n=8) mice (males, B6; 129-Tg (Pcp2-cre)2Mpin/J, 004146, The Jackson Laboratory, Bar

970 Harbor, Maine, bred in-house, 56 days or older). L7-Cre mice express Cre recombinase
971 exclusively in Purkinje neurons[123]. rAAV1-CAG-FLEX-ArchT-GFP (UNC Vector Core, deposited
972 by Dr. Ed Boyden, $4x10^{12}$ vg/ml, AV5593B lot number, 500 nl/injection 250 μm deep perpendicular
973 to tissue) was pressure injected into four locations in lobule VIa/b.

974 Unlike transsynaptic tracing, where each individual animal can be used to test connectivity
975 of a different cerebellar region, this experimental paradigm requires targeting the same cerebellar
976 region (Lobule VI) to achieve sufficient statistical power. To ensure adequate power in this
977 experiment our sample sizes were at least double the size in the original studies developing this
978 methodology[22]. We selected lobule VI as the target, given prior nonmotor findings associated with
979 this lobule[2].

980 After virus injection, a cover slip (round 3 mm, #1 thickness, Warner Instruments 64–0720)
981 was used to cover the craniotomy and a custom titanium plate for head fixation[124] was attached
982 using dental cement (S396, Parkell, Brentwood, NY). Mice were allowed to recover after surgery
983 for 4 weeks and then were habituated to a head-fixed treadmill[124] for three days, 30 minutes per
984 day. On the last day of habituation, ArchT-GFP expression was confirmed using wide-field
985 fluorescence microscopy. The following day, mice were again placed on the treadmill and a 200
986 μm fiber (M200L02S-A, Thorlabs, Newton, NJ) was placed directly over the cranial window for
987 optogenetic stimulation with 532 nm laser (1 Hz, 250 ms pulse-width, 56 mW, 1 hr, GR-532-
988 00200-CWM-SD-05-LED-0, Opto Engine, Midvale, UT). We determined the appropriate
989 stimulation power using test animals, prepared in the same manner as previously described, but
990 also with electrophysiological recordings. We titrated our stimulus on these test animals (not
991 included in manuscript cohort) to ensure it did not produce movements while producing reliable
992 silencing of Purkinje cells during light stimulus, but without significant silencing after termination
993 of the light-stimulus (**Supplementary Figure 20**). The experimental configuration delivered light
994 from illumination from outside the brain, which was therefore attenuated through the air, coverslip,

995 and brain tissue, leading to light scattering and heat dissipation. This made power requirements
996 higher than other published studies[18].

997 We selected the comparison between Cre +/- and Cre -/- animals to ensure our control
998 animals (no Cre, no channelrhodopsin) received the same surgery, injection, coverslip placement,
999 and head mount, and were placed on the same wheel and received the laser placement and
1000 activation. This controlled for differences in experimental stress. These animals were also cage
1001 mates (mixed Cre +/- and Cre -/- in each cage) since birth and provided natural blinding of
1002 condition to the experimenter.

1003 Mice were then individually placed into a clean cage, kept in the dark for one hour, and
1004 perfused as described previously. Brains were fixed overnight in 10% formalin (4% formaldehyde)
1005 before beginning the iDISCO+ clearing protocol. Both ArchT-expressing mice and non-expressing
1006 mice received cranial windows, habituation, and photostimulation.

1007 For behavioral quantification (**Supplementary Figure 20**), videos were imported into
1008 ImageJ using QuickTime for Java library, and images converted into grayscale. Timing of
1009 optogenetic stimulation was confirmed by analysis of pixel intensity over optical fiber connection
1010 to implanted cannulae. Forelimb kinematic data and treadmill speed were analyzed by Manual
1011 Tracking plugin. For arm movement stimulation movements with forearm moving forward (initial
1012 positive slope) from forearm moving backwards (initial negative slope).

1013 **Electrophysiological confirmation of ArchT expression in Purkinje cells.** To confirm that
1014 ArchT was optically activatable in Purkinje cells, photostimulation was done during patch clamp
1015 recording in acutely prepared brain slices. Brain slices were prepared from three 10 week-old
1016 male Pcp2-cre mice (B6.Cg-Tg (Pcp2-cre)3555Jdhu/J, 010536, The Jackson Laboratory), two
1017 weeks after injection with rAAV1-CAG-FLEX-ArchT-GFP. Mice were deeply anesthetized with
1018 Euthasol (0.06 ml/30g), decapitated, and the brain removed. The isolated whole brains were
1019 immersed in ice-cold carbogenated NMDG ACSF solution (92 mM N-methyl D-glucamine, 2.5

1020 mM KCl, 1.25 mM NaH_2PO_4, 30 mM $NaHCO_3$, 20 mM HEPES, 25 mM glucose, 2 mM thiourea,
1021 5 mM Na-ascorbate, 3 mM Na-pyruvate, 0.5 mM $CaCl_2$, 10 mM $MgSO_4$, and 12 mM N-acetyl-L-
1022 cysteine, pH adjusted to 7.3–7.4). Parasagittal cerebellar brain slices 300 μm) were cut using a
1023 vibratome (VT1200s, Leica Microsystems, Wetzlar, Germany), incubated in NMDG ACSF at 34°C
1024 for 15 minutes, and transferred into a holding solution of HEPES ACSF (92 mM NaCl, 2.5 mM
1025 KCl, 1.25 mM NaH_2PO_4, 30 mM $NaHCO_3$, 20 mM HEPES, 25 mM glucose, 2 mM thiourea, 5 mM
1026 Na-ascorbate, 3 mM Na-pyruvate, 2 mM $CaCl_2$, 2 mM $MgSO_4$ and 12 mM N-acetyl-L-cysteine,
1027 bubbled at room temperature with 95% O_2 and 5% CO_2). During recordings, slices were perfused
1028 at a flow rate of 4–5 ml/min with a recording ACSF solution (120 mM NaCl, 3.5 mM KCl, 1.25 mM
1029 NaH_2PO_4, 26 mM $NaHCO_3$, 1.3 mM $MgCl_2$, 2 mM $CaCl_2$ and 11 mM D-glucose) and continuously
1030 bubbled with 95% O_2 and 5% CO_2.
1031 Whole-cell recordings were performed using a Multiclamp 700B (Molecular Devices,
1032 Sunnyvale, CA) using pipettes with a resistance of 3–5 MΩ filled with a potassium-based internal
1033 solution (120 mM potassium gluconate, 0.2 mM EGTA, 10 mM HEPES, 5 mM NaCl, 1 mM $MgCl_2$,
1034 2 mM Mg-ATP and 0.3 mM Na-GTP, pH adjusted to 7.2 with KOH). Purkinje neurons expressing
1035 YFP were selected for recordings. Photostimulation parameters used were 525 nm, 0.12
1036 mW/mm², and 250 ms pulses at 1 Hz.

1037 **Light-sheet microscopy for c-Fos imaging.** Opaque magnets (D1005A-10 Parylene,
1038 Supermagnetman, Pelham, AL) were glued to ventral brain surfaces in the horizontal orientation
1039 and imaged using a light-sheet microscope as described previously. Version 5.1.293 of the
1040 ImSpector Microscope controller software was used. ArchT-GFP injection volumes were acquired
1041 using the 561 nm excitation filter. Cellular imaging of c-Fos expressing cells was acquired using
1042 640 nm excitation filter at 5.0 μm/pixel (1x magnification, 1.3x objective, 0.1 numerical aperture,
1043 9.0 mm working distance, 12.0 x 12.0 mm field of view, LVMI-Fluor 1.3x, LaVision Biotech) with

1044 a 3 μm step-size using a 0.010 excitation NA. This resolution was selected to allow whole-brain
1045 imaging using ClearMap without tiling artifacts. To speed up acquisitions, the autofluorescence
1046 channel and injection channels were acquired separately with a shorter exposure time than the
1047 cell channel. The left and right horizontal focus was shifted towards the side of the emitting sheet.
1048 Left and right images were then sigmoidally blended before analysis. In order to maximize field of
1049 view, some olfactory areas were not completely represented in images and were removed from
1050 analysis. Five brains were reimaged a second time due to ventricular imaging artifacts.

1051 **Automated detection of c-Fos expressing cells.** Detection of c-Fos expressing cells after
1052 optogenetic stimulation was done using ClearMap software for c-Fos detection[22] modified to run
1053 on high performance computing clusters ("ClearMapCluster", see **Table 5** for analysis
1054 parameters). Cell detection parameters were optimized by two users iterating through a set of
1055 varying ClearMap detection parameters and selecting those that minimized false positives while
1056 labelling only c-Fos positive neurons with high signal-to-noise ratio.

1057 **Statistical analysis of c-Fos data.** Cell and density heat maps and p-value maps were
1058 generated using ClearMap. Projected p-value maps were generated by binarizing the p-value
1059 maps and counting non-zero voxels in z; color bar thresholding displayed greater than 25% for
1060 coronal and 27% for sagittal sections of the z-distance. Injection sites were segmented and
1061 aligned in the manner described previously. Activation ratio was defined as the mean number of
1062 cells in an anatomical area across experimental brains divided by the mean number of cells in the
1063 same anatomical area in control brains. To compare the c-Fos activation data with transsynaptic
1064 tracing data across the major divisions in the neocortex, linear-least squares regression
1065 (scipy.stats.linregress, two-sided) were calculated using mean viral-labeling neocortical densities
1066 with H129-VC22 injections (80 hpi) were compared with the mean cell density ratio of c-Fos
1067 stimulation vs control groups.

1068 **SOFTWARE**

1069 Data analysis pipelines were run using custom code written for Python 3+ (available at
1070 github.com/PrincetonUniversity/BrainPipe and github.com/PrincetonUniversity/ClearMapCluster)
1071 Unless otherwise noted, analyses and plotting were performed in Python 2.7+. DataFrame
1072 manipulations were done using Numpy[125] 1.14.3 and Pandas[126] 0.23.0. Plotting was done with
1073 Matplotlib[127] 2.2.2 and Seaborn[128] 0.9.0. Image loading, manipulation and visualization was done
1074 using Scikit-Image[116] 0.13.1 and SimpleITK[129] 1.0.0. SciPy[113] 1.1.0 was used for statistical
1075 analyses. Clustering analysis was performed using Seaborn[128] 0.9.0 and Scikit-Learn[130] 0.19.1
1076 was used for hierarchical agglomerative clustering (average metric, Ward's method). Coefficients
1077 and standard errors for the generalized linear model were obtained by fitting the model using the
1078 statsmodels 0.9.0 package in Python 3.7.1 (as in Ref. 2). The Mann-Whitney U test (two-tailed;
1079 scipy.stats.mannwhitneyu, SciPy[113] 1.1.0) was used to determine statistical significance between
1080 control and experimental brain regions in c-Fos studies.

ACKNOWLEDGMENTS

We thank Aleksandra Badura for advice on experimental design, Lynn W. Enquist for discussion and for the generous gift of PRV-Bartha 152 (CNNV, P40 OD010996), James Gornet for neural network implementation assistance, Austin Hoag for software design and management, Nicolas Renier and Kelly Seagraves for tissue-clearing optimization, Stephan Thiberge for microscopy help, and Shruthi Deivasigamani, Joseph Gotto, Joyce C. Lee, Laura A. Lynch, Caroline Jung, Dafina Pacuku, and Thaddeus Weigel for technical assistance. This work was supported by NIH R01 NS045193, R01 MH115750, and U19 NS104648 (S.W.), F31 NS089303 (T.P.), P40 OD010996 (E.E.), R21 DC018365 (B.R.), and P20GM103408 (E.H. and B.R.), Netherlands Organization for Scientific Research - Veni ZonMW, 91618112 (H.-J.B), Erasmus MC Fellowship 106958 (H.-J.B), and the New Jersey Council on Brain Injury Research (J.V.) .

AUTHOR CONTRIBUTIONS

T.P., M.K., H.-J.B., and S.W. conceived and designed the experiments. T.P., D.B., and J.V. performed virus injections and prepared tissue. Z.D. and T.P. imaged tissue and ran the computational data analysis pipeline for whole-brain imaging data. T.P., Z.D., and H.-J. B. performed subsequent data analysis and prepared figures. E.E. designed and provided HSV vectors. K.U.V. and T.P. designed algorithms for image analysis. M.K., J.L., and T.P. performed optogenetics experiments. E.H. and B.R. performed AAVrg experiments, B.R. collected and analyzed images. H.-J. B., N. de O. and F.H. performed AAV experiments and collected and analyzed images. T.P. and S.W. wrote the initial draft of the manuscript, which was edited by all authors.

COMPETING INTERESTS

The authors declare that they have no competing interests.

DATA AVAILABILITY

The datasets generated and analyzed in the current study are available from the corresponding author upon request.

CODE AVAILABILITY

All experimental and analysis code is available at the links provided in the Methods section.

FIGURES

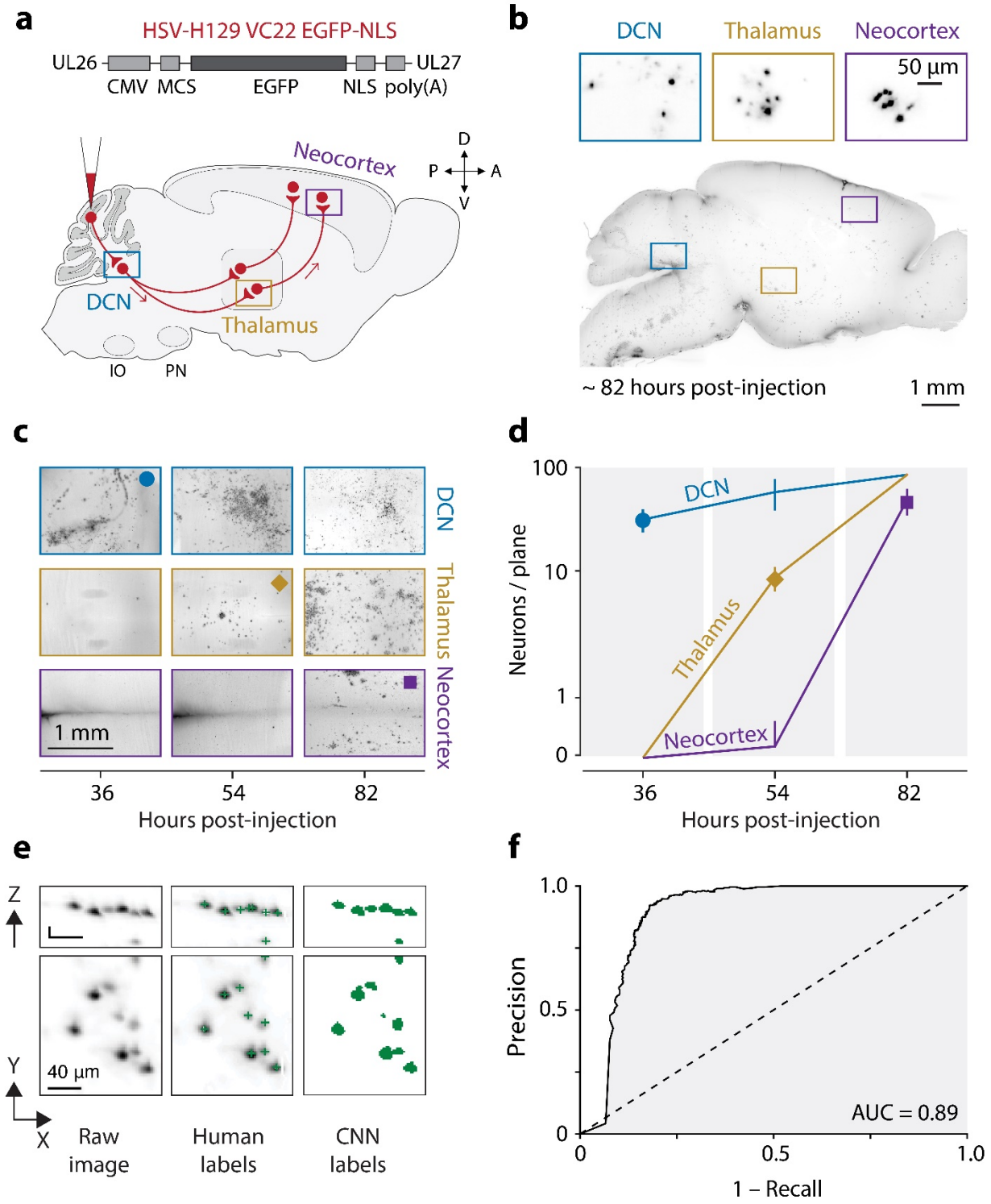

Figure 1. Large-scale transsynaptic tracing with tissue clearing and light-sheet microscopy. (a) *Top,* H129-VC22, a recombinant HSV-H129 virus that expresses a nuclear location signal tagged to an enhanced green fluorescent protein (EGFP). *Bottom,* experimental

design to transsynaptically trace pathways from cerebellar cortex to thalamus and neocortex. (b) Example images of an iDISCO+ cleared brain ~82 hours post-injection. 158 μm maximum intensity projection. (c) Time course of infection. Images show horizontal maximum intensity projections of iDISCO+ cleared brains in the cerebellar nuclei (3.0 mm dorsal of bregma), thalamus (3.0 mm dorsal), and neocortex (0.7 mm dorsal). Dorsoventral depth of projection: 300 μm for cerebellar nuclei and thalamus, 150 μm for neocortex. (d) Quantification of viral spread. Quantification of cell counts from five planes at each timepoint for each brain region is shown. Error bars represent 95% confidence interval. (e) Training data for convolutional neural network (CNN). *Left,* representative images of raw input data. *Middle,* human-annotated cell centers (green overlay) for training the network. *Right,* segmented labels (green) used as training input. (f) Receiver operating characteristic curve for the trained neural net. The diagonal line indicates chance performance.

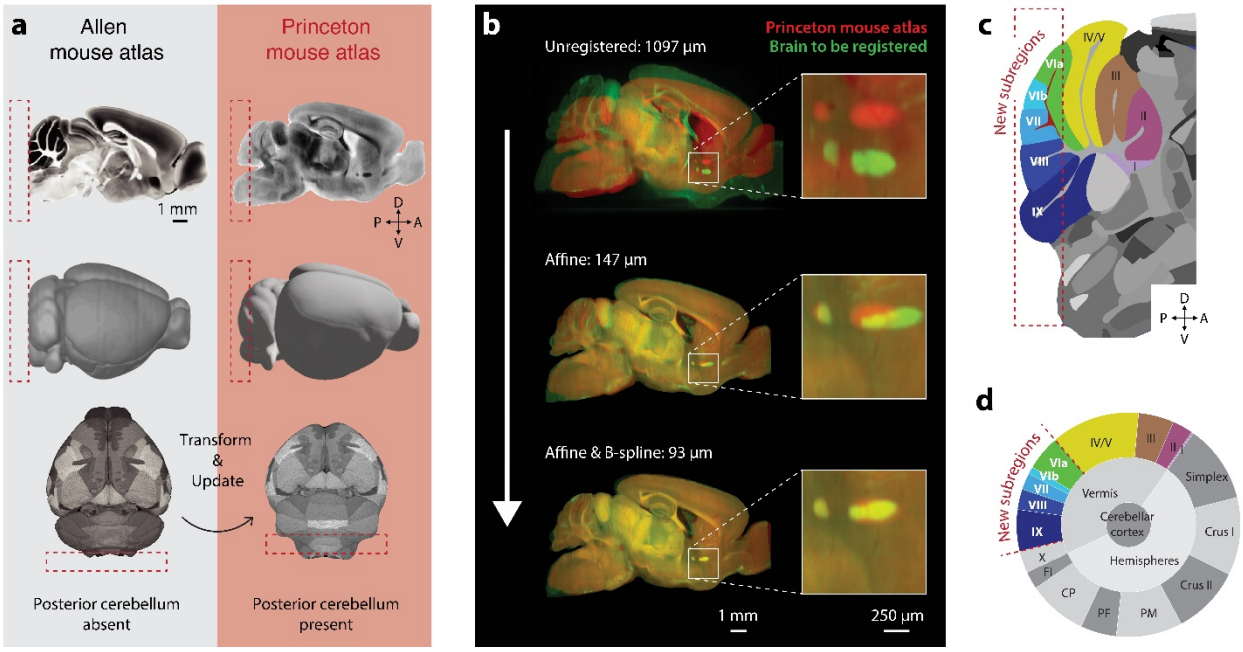

Figure 2. The Princeton Mouse Brain Atlas for light-sheet volume registration. (a) Sagittal views demonstrate differences between Allen Brain Atlas (ABA, left) and the Princeton Mouse Brain Atlas (PMA, right). The red dotted box indicates the caudal limit of the ABA. To map between PMA and ABA space, ABA annotations were transformed into PMA space. (b) Registration of whole-brain light-sheet volumes to the PMA. Light-sheet volume of an individual brain (green) overlaid with PMA (red) at different stages of registration. Median discrepancy is shown for each stage of alignment. (c) PMA cerebellar annotations. The red dotted box indicates newly annotated areas. (d) PMA cerebellar hierarchy depicting structure ontology and shows relative substructure size contributions. Abbreviations: PM, paramedian lobule; PF, paraflocculi; CP, copula pyramidis; Fl, flocculus.

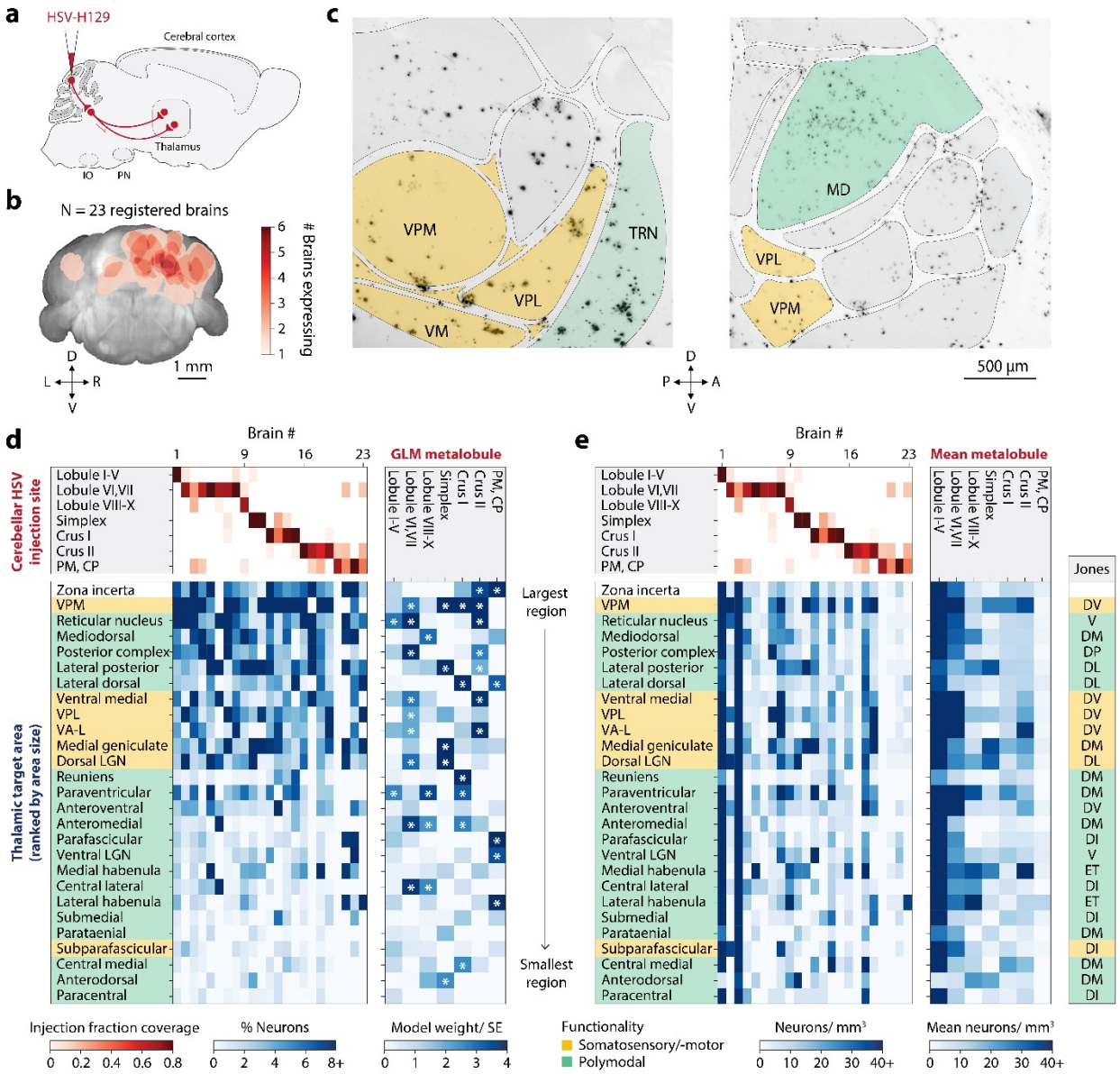

Figure 3. Cerebellar paths to thalamus. (a) Disynaptic path from the cerebellar cortex to thalamus traced using H129-VC22. (b) Coverage of cerebellum by thalamic timepoint injections. Coronal projections show the number of injections covering each location. (c) Example sagittal image of labeling ~54 hours post-injection, with outlines defining key thalamic nuclei. 150 µm maximum intensity projection. (d) *Left*, fraction of neurons across all injection sites. Percentage fraction was calculated by dividing the number of neurons detected by the total number of neurons detected across all thalamus. Injection coverage fractions (red) and fraction of neurons (blue) are represented. One column represents one mouse. *Right*, a generalized linear model showing the influence of each cerebellar region on thalamic expression. The heatmap (blue) represents the coefficient divided by the standard error. Significant coefficients are marked with asterisks. (e) *Left*, density of neurons in each thalamic area across all cerebellar injection sites. *Middle*, mean density projections across injections sites from the same cerebellar region. *Right*, grouping according to Ref. 30. Abbreviations: VPM, ventral posteromedial; VA-L, ventral anterior-lateral; VPL, ventral posterolateral; LGN, lateral geniculate nucleus.

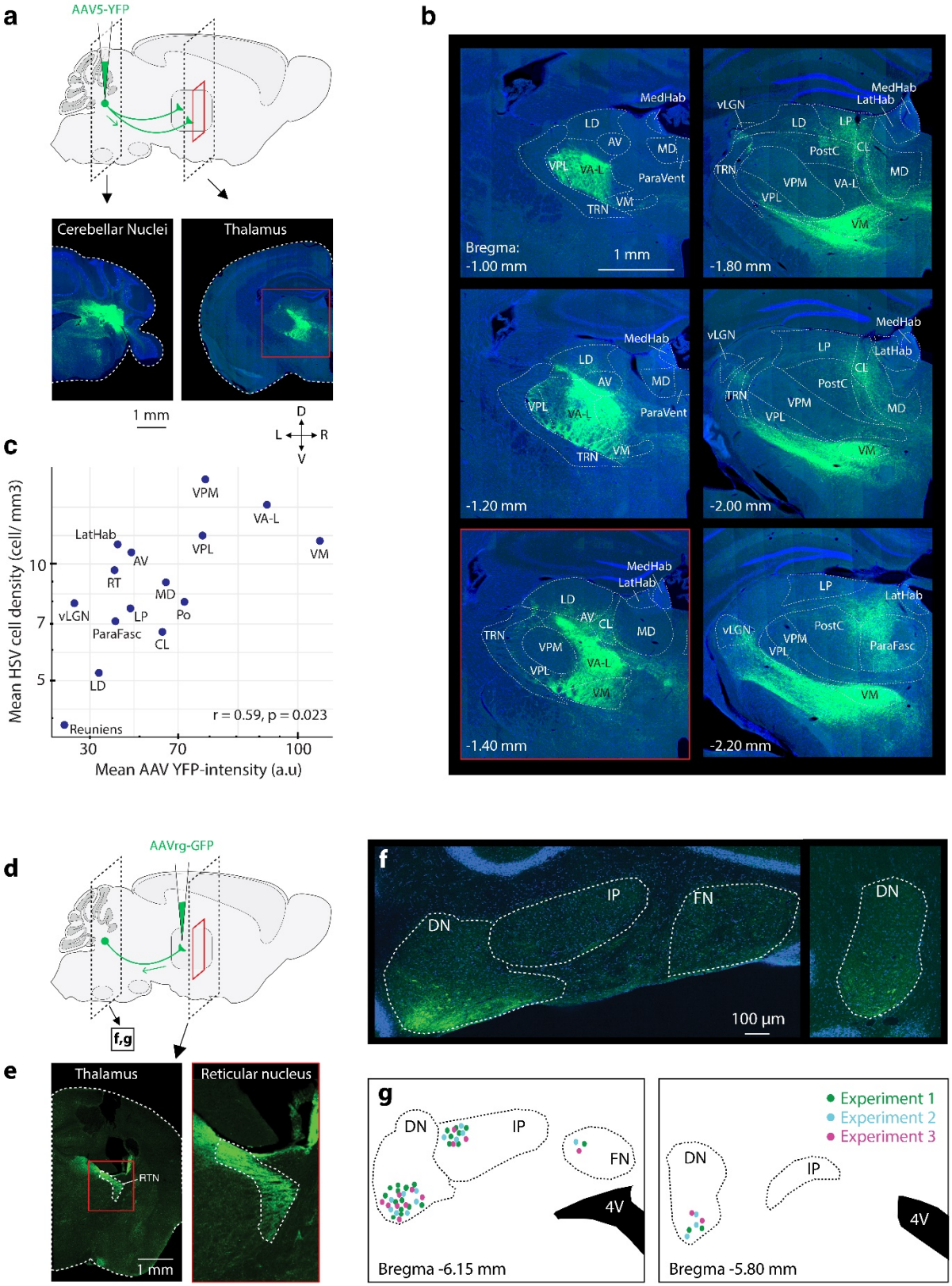

Figure 4. Cerebellothalamic AAV-identified axonal projections correspond with transsynaptic viral tracing including the thalamic reticular nucleus. (a) Cerebellar nuclei

were injected with AAV-YFP. Brains were coronally sectioned to identify cerebellothalamic axonal projection density. (b) Coronal sections after a cerebellar nuclear injection primarily targeting the interpositus and dentate nuclei. Manually drawn Paxinos coronal overlays are shown. Bregma -1.40 mm corresponds to A. (c) Cerebellothalamic axons identified by AAV injections aligned with transsynaptic tracing. Pearson's correlation ($r=0.59$, $p=0.023$) of rank order density of HSV-labeled thalamic neurons after cerebellar cortical injection versus cerebellothalamic axonal projection density. (d) Schematic of AAVrg-hSyn-Chronos-GFP (AAVrg-GFP) injection into right TRN. (e) Confocal microscopy image of AAVrg-GFP expression in TRN (outlined in white). Co-labeling of GFP (green) that labels a major subset of TRN neurons. (f) Example confocal microscopy images from the left cerebellar nuclei demonstrate presence of GFP-expressing (green) neuron bodies primarily in the ventrolateral dentate with additional expression in dorsal IP and fastigial nuclei. Nuclei are labeled with Hoechst (blue). (g) Distribution of GFP+ neuronal cell bodies (dot) throughout the cerebellar nuclei quantified from 4-5 coronal cerebellar sections per animal with GFP-expressing neurons color-coded to correspond to individual experiments. Abbreviations: 4V, fourth ventricle; AV, anteroventral; CL, central lateral; DN, dentate nucleus; FN, fastigial nucleus; GFP, green fluorescent protein; Hip, hippocampus; IP, interpositus nucleus; LatHab, lateral habenula; LD, lateral dorsal; LP, lateral posterior; M, motor cortex; MD, mediodorsal; ParaFasc, parafascicular; Po, posterior complex; PV, parvalbumin; S, somatosensory cortex; TRN, thalamic reticular nucleus; VA-L, ventral anterior-lateral; VM, ventral medial; VN, vestibulocerebellar nucleus; VPL, ventral posterolateral; VPM, ventral posteromedial; vLGN, ventral lateral geniculate nucleus; ZI, zona incerta.

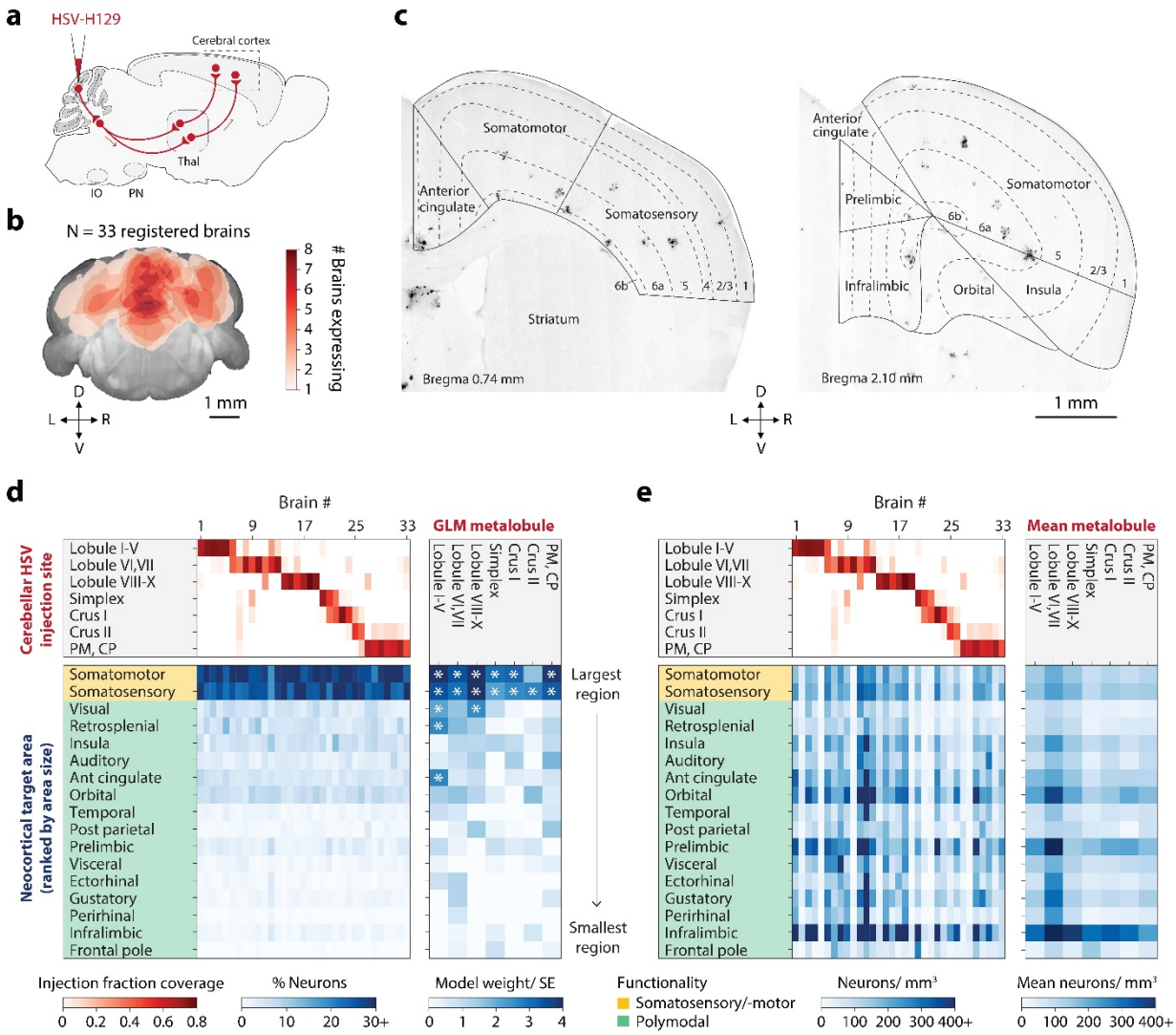

Figure 5. Cerebellar paths to neocortex. (a) The trisynaptic path from the cerebellar cortex to the neocortex traced using H129-VC22. (b) Coverage of cerebellum by neocortical timepoint injections. Coronal projections show the number of injections covering each cerebellar location. (c) Example coronal image of labeling ~80 hours post-injection. 100 µm maximum intensity projection. (d) *Left*, fraction of neurons in each neocortical area across all injection sites. Injection coverage fractions (red) and fraction of neurons (blue) are represented for each brain injected. Brains are ordered by primary injection site. *Right*, a generalized linear model showing the influence of each cerebellar region on neocortical expression. The heatmap (blue) represents the coefficient divided by the standard error. Significant coefficients are marked with asterisks. (e) *Left*, density of neurons in each neocortical area across all injections. *Right*, mean density of neurons. Abbreviations: Ant, anterior; CP, Copula pyramidis; PM, Paramedian; Post, posterior.

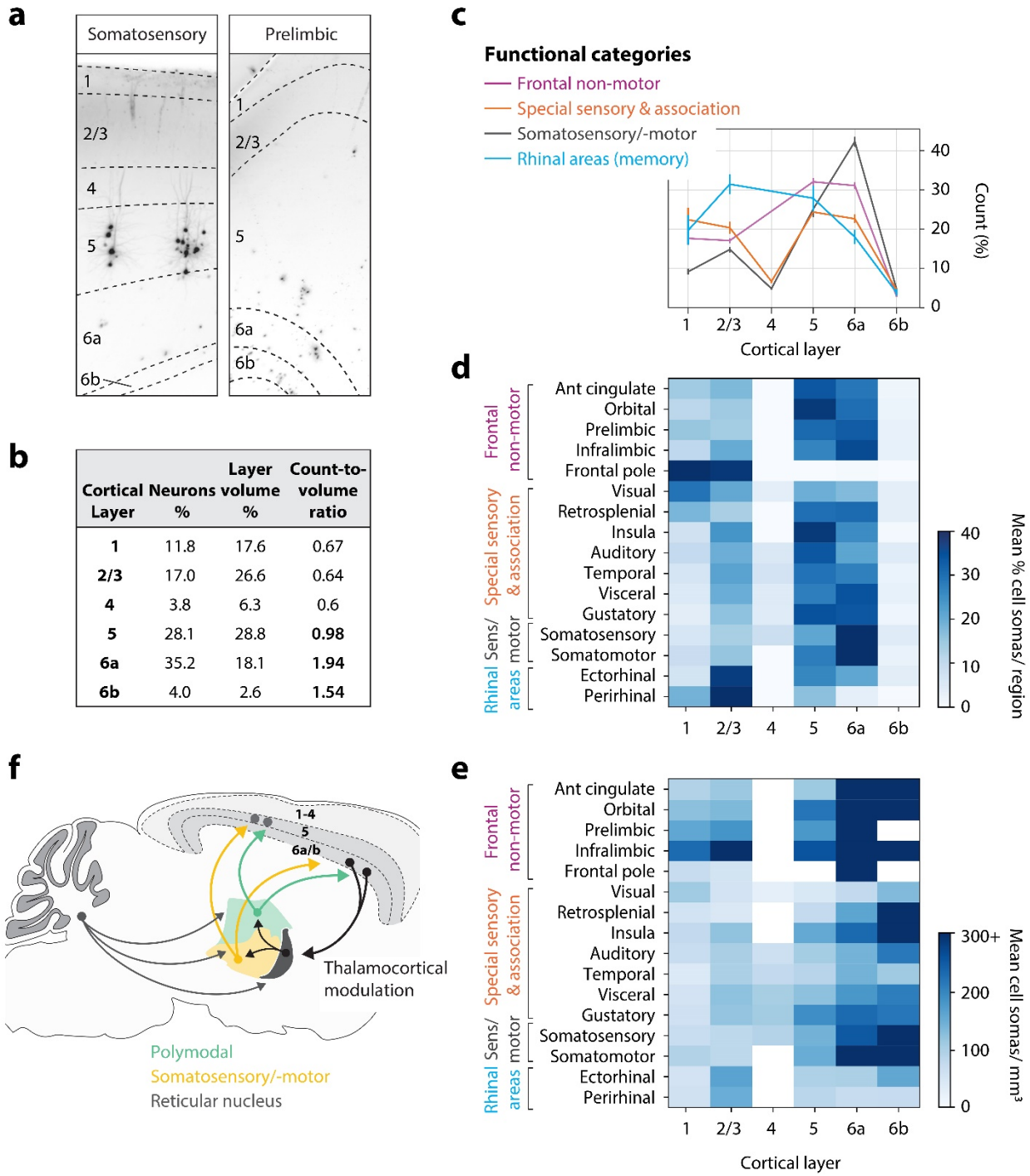

Cortical Layer	Neurons %	Layer volume %	Count-to-volume ratio
1	11.8	17.6	0.67
2/3	17.0	26.6	0.64
4	3.8	6.3	0.6
5	28.1	28.8	**0.98**
6a	35.2	18.1	**1.94**
6b	4.0	2.6	**1.54**

Figure 6. Cerebellar projections to thalamocortical and deep-layer modulatory systems. (a) Example images of labeling in the neocortex ~80 hours post-injection, with outlines defining neocortical layers in each area. 75 µm maximum intensity projections. (b) Distribution of neocortical neurons in layers by neocortical area. *Top*, mean percentage of neurons normalized by area. *Bottom*, mean density of neurons. (c) Projection differences by layer after grouping cortical regions by function. Percent of cortical neurons shown. (d) Average percent of HSV-H129 neurons per region and (e) average density for neocortical regions separated by layer. Neocortical regions are functionally grouped as in (c). (f) Summary of cerebellar output connectivity to

thalamus and neocortex demonstrated by transsynaptic tracing. Thalamic targets include sensory relay nuclei, polymodal association nuclei, and the reticular nucleus. Abbreviations: Ant, anterior. Functional categories: Rhinal: perirhinal and ectorhinal areas; Somatosensory/-motor: somatosensory and somatomotor areas; Special sensory & association: retrosplenial, visual, gustatory, visceral, auditory, and temporal association areas; Frontal nonmotor: infralimbic, anterior cingulate, orbital, prelimbic, agranular insular areas.

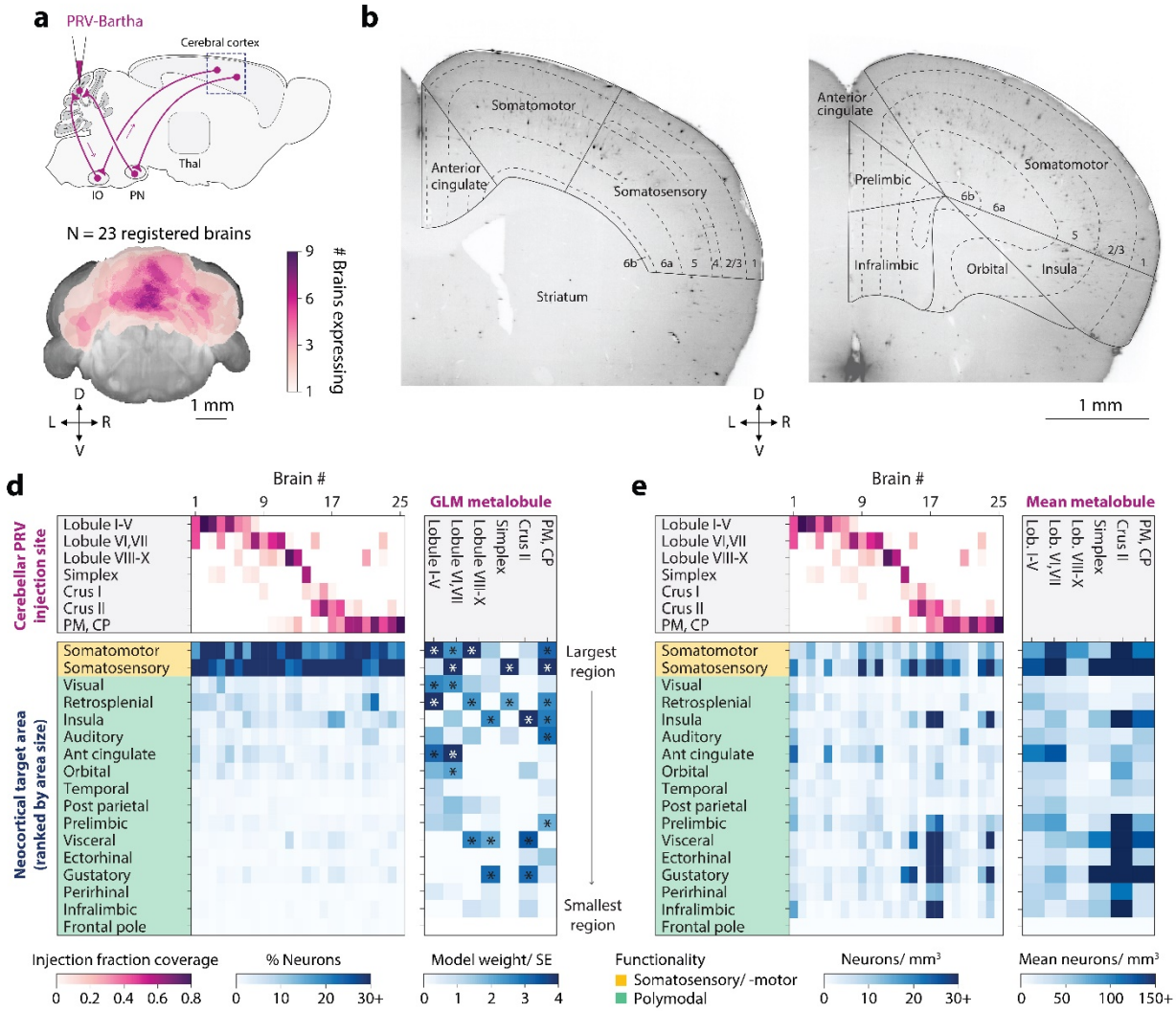

Figure 7. Descending projections to cerebellar cortex labeled using PRV-Bartha. (a) Schematic of the retrograde disynaptic path from the cerebellar cortex to the neocortex traced using PRV-Bartha. (b) Coverage of cerebellum by neocortical timepoint injections. Coronal projections show the number of injections covering each cerebellar location. (c) Example sagittal image of typical labeling ~80 hours post-injection. 375 µm maximum intensity projection. (d) *Left*, fraction of neurons in each neocortical area across all injection sites. The percentage fraction was calculated by dividing the number of neurons detected in each area by the total number of neurons detected in neocortex. Injection coverage fractions (pink) and fraction of neurons (blue) are represented for each brain injected. *Right*, a generalized linear model showing the influence of each cerebellar region on neocortical expression. The heatmap (blue) represents the coefficient divided by the standard error. Significant coefficients are marked with asterisks. (e) *Left*, density of neurons in each neocortical area across all cerebellar injection sites. *Right*, mean density of neurons in each neocortical area grouped by primary injection site.

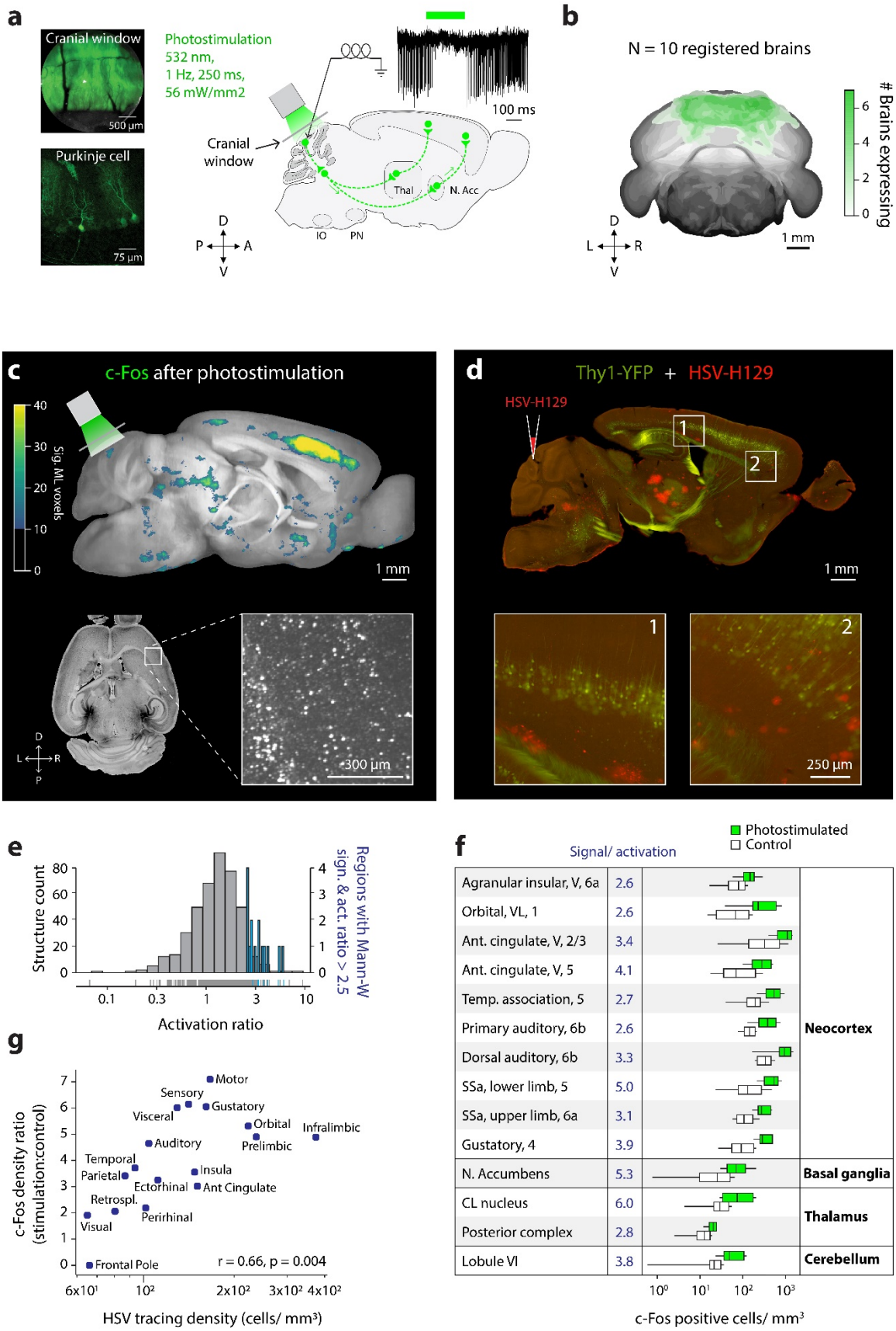
a
Cranial window
500 µm
Purkinje cell
75 µm
Photostimulation
532 nm,
1 Hz, 250 ms,
56 mW/mm2
100 ms
Cranial window
Thal
N. Acc
IO
PN
D
P
A
V
b
N = 10 registered brains
# Brains expressing
6
4
2
0
1 mm
D
L
R
V
c
c-Fos after photostimulation
Sig. ML voxels
40
30
20
10
0
1 mm
300 µm
D
L
R
P
d
Thy1-YFP + HSV-H129
HSV-H129
1
2
1 mm
250 µm
e
Structure count
80
60
40
20
0
Regions with Mann-W sign. & act. ratio > 2.5
4
3
2
1
0
0.1
0.3
1
3
10
Activation ratio
f
Signal/ activation
Photostimulated
Control
Agranular insular, V, 6a 2.6
Orbital, VL, 1 2.6
Ant. cingulate, V, 2/3 3.4
Ant. cingulate, V, 5 4.1
Temp. association, 5 2.7
Primary auditory, 6b 2.6
Dorsal auditory, 6b 3.3
SSa, lower limb, 5 5.0
SSa, upper limb, 6a 3.1
Gustatory, 4 3.9
N. Accumbens 5.3
CL nucleus 6.0
Posterior complex 2.8
Lobule VI 3.8
Neocortex
Basal ganglia
Thalamus
Cerebellum
10⁰
10¹
10²
10³
c-Fos positive cells/ mm³
g
c-Fos density ratio (stimulation:control)
7
6
5
4
3
2
1
0
Motor
Sensory
Gustatory
Visceral
Orbital
Infralimbic
Prelimbic
Auditory
Temporal
Parietal
Insula
Ectorhinal
Ant Cingulate
Retrospl.
Perirhinal
Visual
Frontal Pole
r = 0.66, p = 0.004
6x10¹
10²
2x10²
3x10²
4x10²
HSV tracing density (cells/ mm³)

Figure 8. Cerebellar perturbation activates transsynaptically connected regions across the brain. (a) Experimental setup for photostimulating the inhibitory optogenetic protein ArchT-GFP through a cranial window over cerebellar lobule VI. *Top*, silencing of Purkinje cells as measured in brain-slice whole-cell recordings after photostimulation with 525 nm light. (b) Coverage of cerebellum by ArchT-GFP expression. Coronal projections show the number of injections covering each cerebellar location. (c) Neural activity identified by c-Fos immunostaining. *Top*, voxel-by-voxel regions of statistically significant c-Fos activation in Princeton Mouse Atlas (PMA) space (planes 320-360, 20 μm isotropic voxel size). *Bottom*, example horizontal image of typical c-Fos labeling after optogenetic perturbation. 132 μm maximum intensity projection. (d) Transsynaptic targets of lobule VI labeled using H129-VC22 (red) injected into Thy1-YFP (green) mice. Standard non-clearing histological imaging, 50 μm section, 80 hpi. (e) Activation ratios, defined by the number of c-Fos neurons in the photostimulated divided by the control-group, for all brain regions. Regions were scored as responding (blue coloring) if they had activation ratios greater than 2.5 and $p<0.05$ by two-tailed Mann-Whitney test. (f) Distribution of c-Fos neurons for all responding regions. (g) c-Fos density ratio (mean stimulation density divided by mean control density) is positively correlated ($r=0.66$) with neocortical transsynaptic tracing density. For boxplots, center line represents median; box limits, upper and lower quartiles; whiskers, 1.5 times the interquartile range. Abbreviations: Ant, Anterior; C, caudal; D, dorsal; N, nucleus; Retrospl., retrosplenial area; SM, somatomotor areas; SS, somatosensory areas; V, ventral.

Largest amount of cerebellar output

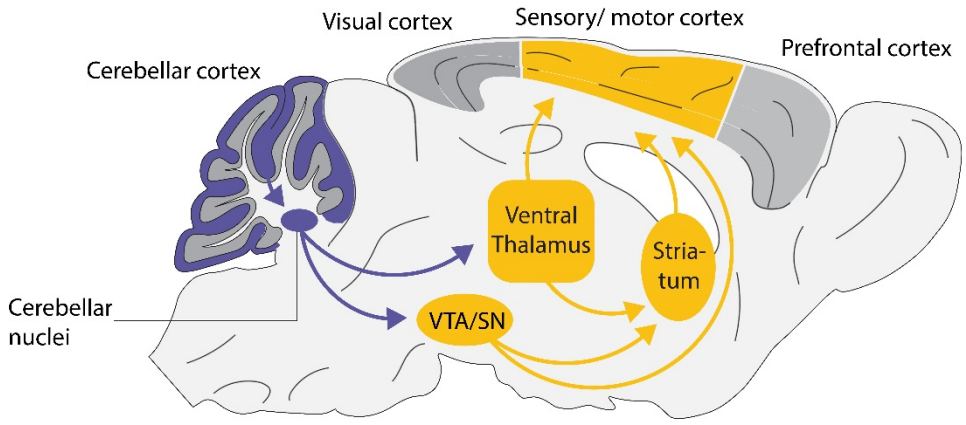

Most concentrated cerebellar output

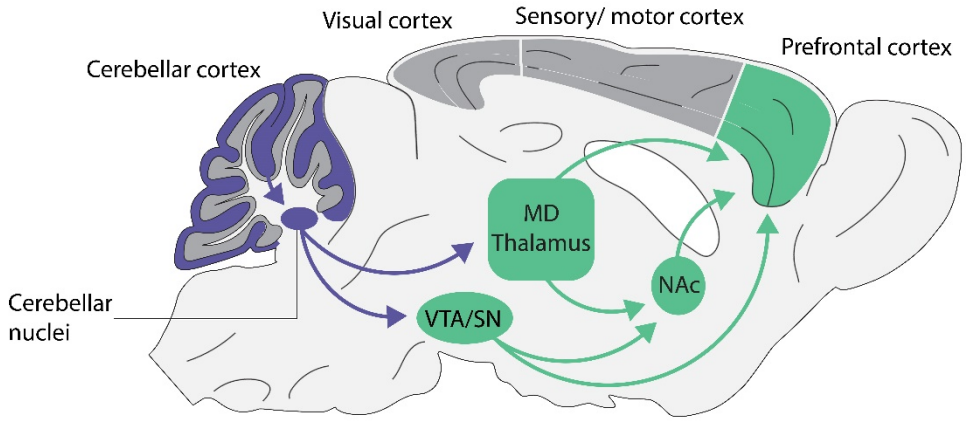

Thalamocortical modulation

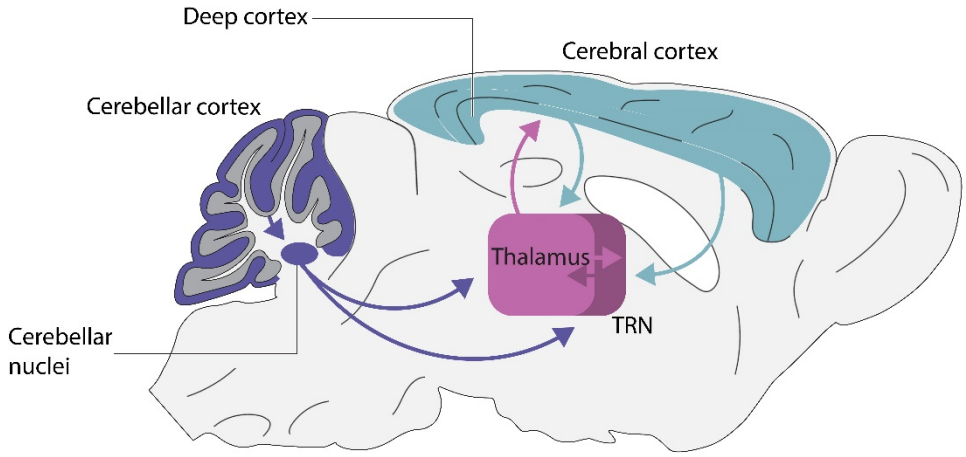

Figure 9. Parallel ascending cerebellar pathways for sensorimotor, associative, and regulatory function. *Top*, the most cerebellar projections in thalamus and neocortex are found in sensorimotor structures. *Middle*, the densest cerebellar projections are found in frontal neocortical structures. *Bottom*, the cerebellum projects to thalamocortical regions involved in sensory modulation, attentional selection[109], and control of processing[110].

Table 1. Cohort details for each structure analyzed. Abbreviations: hpi, hours post-injection.

Structure	Timepoint	Number of brains	Edge erosion	Ventricular erosion
Brainstem (H129)	28-36 hpi	5	60 µm	80 µm
Thalamus (H129)	54 hpi	23	60 µm	80 µm
Neocortex (H129)	80 hpi	33	60 µm	80 µm
Striatum (H129)	80 hpi	33	60 µm	80 µm
Hypothalamus (H129)	80 hpi	31	60 µm	160 µm
Neocortex (PRV)	80 hpi	25	60 µm	80 µm

Table 2. Training datasets descriptions used to train cell detectors.

CNN	Different brains	Different volumes	Number of cells	Human-CNN concordance	Human-human concordance
H129	8	44	3603	F1: 0.864 Precision: 0.912 Recall: 0.821	F1: 0.891 Precision: 0.947 Recall: 0.842 1091 cells annotated by both users
PRV	7	41	5119	F1: 0.873 Precision: 0.833 Recall: 0.926	F1: 0.886 Precision: 0.936 Recall: 0.841 1280 cells annotated by both users

Table 3. Thalamic target area function references. Abbreviations: VA-L, ventral anterior-lateral; VPL, ventral posterolateral; VPM, ventral posteromedial; LGN, lateral geniculate nucleus.

Thalamic Area	General function	Reference
Anteroventral	Spatial Memory	131
Central lateral	Emotional aspects of nociception	132
Lateral dorsal	Somatosensory processing	133
Lateral posterior	Visually-guided behavior	134
Lateral habenula	Reward Negative	135
Mediodorsal	Processing/integration of memory/cognition	34
Medial habenula	Emotion-associated behavior	136
Parafascicular	Reversal Learning	137
Paraventricular	Emotional arousal, +/- behavioral mediation	62,138
Posterior triangle	Nociception	139
Posterior complex	Adjusting response to unexpected sensory input	140
Reticular	Cortical-based modulation of thalamus	74
Reuniens	Hippocampal modulation	141
Submedial	Olfaction	142
VA-L	Memory/Spatial navigation & Motor	143
Ventral medial	Motor	144
VPL	Sensory Body	145
VPM	Sensory Face	145
Ventral LGN	Visuomotor response & Circadian rhythms	146

Table 4. Experimental injection and clearing protocols for transsynaptic and physiologic tracing from cerebellum. Abbreviations: hpi, hours post-injection.

Target	Injection	Primary antibody	Secondary antibody
c-Fos	rAAV1-CAG-FLEX-ArchT-GFP	1:2000 Rabbit anti-c-Fos Synaptic Systems Cat. No. 226003	1:500 Donkey anti-Rabbit AlexaFluor 790 ThermoFisher A11374
Anterograde thalamic timepoint (28-36 hpi)	H129-VC22 ($2.7x10^4$ to $8.0x10^4$ PFUs)	1:1750 Rabbit anti-HSV Dako B011402-2	1:500 Donkey anti-Rabbit AlexaFluor 647 ThermoFisher A31573
Anterograde thalamic timepoint (54 hpi)	H129-VC22 ($2.7x10^4$ to $8.0x10^4$ PFUs)	1:1750 Rabbit anti-HSV Dako B011402-2	1:500 Donkey anti-Rabbit AlexaFluor 647 ThermoFisher A31573
Anterograde neocortical timepoint (80 hpi)	H129-VC22 ($2.7x10^4$ to $8.0x10^4$ PFUs)	1:350 Rabbit anti-HSV Dako B011402-2	1:250 Donkey anti-Rabbit AlexaFluor 647 ThermoFisher A31573
Retrograde neocortical timepoint (28-50 hpi)	PRV-Bartha 152 ($6.0x10^4$ PFUs)	1:750 Chicken anti-GFP Aves GFP-1020	1:400 Donkey anti-Chicken AlexaFluor 647 Jackson ImmunoResearch 703-606-155
Retrograde neocortical timepoint (80 hpi)	PRV-Bartha 152 ($6.0x10^4$ PFUs)	1:500 Chicken anti-GFP Aves GFP-1020	1:300 Donkey anti-Chicken AlexaFluor 647 Jackson ImmunoResearch 703-606-155

Table 5. ClearMap parameters used on whole-brain light-sheet volumes for detecting c-Fos positive neurons.

ClearMap parameter	Value
`removeBackgroundParameter_size`	(5,5)
`findExtendedMaximaParameter_size`	(5,5)
`findExtendedMaximaParameter_threshold`	0
`findIntensityParameter_size`	(3,3,3)
`detectCellShapeParameter_threshold`	105

Table 6. HSV-H129 timepoints used in transsynaptic tracing studies.

H129 Publication	Circuit	Timepoint (hours post injection)
147	Airway related-sensory circuitry (1 synapse)	48 hours (no expression at 24 hours).
25	White adipose tissue to CNS (1 synapse)	48 hr (no expression at 24 hr)
44	DCN -> midbrain (1 synapse)	50 hr
Our study	**Cerebellum -> DCN -> midbrain (2 synapses)**	**54 hr**
2	Cerebellum -> DCN -> midbrain (2 synapses)	60 hr
25	White adipose tissue to CNS (2 synapses)	72 hr
148	Tracheal sensory pathways (peripheral nervous system -> CNS 2 synapses at 72hr, 3 at 96hr)	72 hr (also 96-144 hr)
2	Cerebellar -> DCN -> thalamus -> neocortex (3 synapses)	80 hr
149	Cerebellar output to neocortex (3 synapses)	96 hours

REFERENCES

1. Stoodley, C. J. & Schmahmann, J. D. Functional topography in the human cerebellum: a meta-analysis of neuroimaging studies. *Neuroimage* **44**, 489–501 (2009).
2. Badura, A. *et al.* Normal cognitive and social development require posterior cerebellar activity. *Elife* **7**, (2018).
3. Deverett, B., Koay, S. A., Oostland, M. & Wang, S. S.-H. Cerebellar involvement in an evidence-accumulation decision-making task. *Elife* **7**, (2018).
4. Courchesne, E. *et al.* Unusual brain growth patterns in early life in patients with autistic disorder: an MRI study. *Neurology* **57**, 245–254 (2001).
5. Limperopoulos, C. *et al.* Does cerebellar injury in premature infants contribute to the high prevalence of long-term cognitive, learning, and behavioral disability in survivors? *Pediatrics* **120**, 584–593 (2007).
6. Wang, S. S.-H., Kloth, A. D. & Badura, A. The cerebellum, sensitive periods, and autism. *Neuron* **83**, 518–532 (2014).
7. Clark, D. A., Mitra, P. P. & Wang, S. S. Scalable architecture in mammalian brains. *Nature* **411**, 189–193 (2001).
8. Voogd, J. & Ruigrok, T. J. H. Chapter 15 - Cerebellum and Precerebellar Nuclei. in *The Human Nervous System (Third Edition)* (eds. Mai, J. K. & Paxinos, G.) 471–545 (Academic Press, 2012). doi:10.1016/B978-0-12-374236-0.10015-X.
9. Percheron, G., François, C., Talbi, B., Yelnik, J. & Fénelon, G. The primate motor thalamus. *Brain Res. Brain Res. Rev.* **22**, 93–181 (1996).
10. Ruigrok, T. J. H., Sillitoe, R. V. & Voogd, J. Chapter 9 - Cerebellum and Cerebellar Connections. in *The Rat Nervous System (Fourth Edition)* (ed. Paxinos, G.) 133–205 (Academic Press, 2015). doi:10.1016/B978-0-12-374245-2.00009-7.
11. Strick, P. L., Dum, R. P. & Fiez, J. A. Cerebellum and nonmotor function. *Annu. Rev. Neurosci.* **32**, 413–434 (2009).

12. Voogd, J. & Ruigrok, T. J. H. The organization of the corticonuclear and olivocerebellar climbing fiber projections to the rat cerebellar vermis: the congruence of projection zones and the zebrin pattern. *J. Neurocytol.* **33**, 5–21 (2004).
13. Apps, R. & Hawkes, R. Cerebellar cortical organization: a one-map hypothesis. *Nat. Rev. Neurosci.* **10**, 670–681 (2009).
14. Sugihara, I. & Shinoda, Y. Molecular, topographic, and functional organization of the cerebellar cortex: a study with combined aldolase C and olivocerebellar labeling. *J. Neurosci.* **24**, 8771–8785 (2004).
15. Suzuki, L., Coulon, P., Sabel-Goedknegt, E. H. & Ruigrok, T. J. H. Organization of cerebral projections to identified cerebellar zones in the posterior cerebellum of the rat. *J. Neurosci.* **32**, 10854–10869 (2012).
16. Popa, T., Russo, M. & Meunier, S. Long-lasting inhibition of cerebellar output. *Brain Stimul.* **3**, 161–169 (2010).
17. Buckner, R. L., Krienen, F. M., Castellanos, A., Diaz, J. C. & Yeo, B. T. T. The organization of the human cerebellum estimated by intrinsic functional connectivity. *J. Neurophysiol.* **106**, 2322–2345 (2011).
18. Choe, K. Y., Sanchez, C. F., Harris, N. G., Otis, T. S. & Mathews, P. J. Optogenetic fMRI and electrophysiological identification of region-specific connectivity between the cerebellar cortex and forebrain. *Neuroimage* **173**, 370–383 (2018).
19. Aoki, S., Coulon, P. & Ruigrok, T. J. H. Multizonal Cerebellar Influence Over Sensorimotor Areas of the Rat Cerebral Cortex. *Cereb. Cortex* **29**, 598–614 (2017).
20. Middleton, F. A. & Strick, P. L. Cerebellar output: motor and cognitive channels. *Trends Cogn. Sci.* **2**, 348–354 (1998).
21. Dum, R. P. & Strick, P. L. Transneuronal tracing with neurotropic viruses reveals network macroarchitecture. *Curr. Opin. Neurobiol.* **23**, 245–249 (2013).
22. Renier, N. *et al.* Mapping of Brain Activity by Automated Volume Analysis of Immediate

Early Genes. *Cell* **165**, 1789–1802 (2016).

23. Teune, T. M., van der Burg, J., van der Moer, J., Voogd, J. & Ruigrok, T. J. Topography of cerebellar nuclear projections to the brain stem in the rat. *Prog. Brain Res.* **124**, 141–172 (2000).
24. Wijesinghe, R., Protti, D. A. & Camp, A. J. Vestibular Interactions in the Thalamus. *Front. Neural Circuits* **9**, 79 (2015).
25. Song, C. K., Kay Song, C., Schwartz, G. J. & Bartness, T. J. Anterograde transneuronal viral tract tracing reveals central sensory circuits from white adipose tissue. *American Journal of Physiology-Regulatory, Integrative and Comparative Physiology* vol. 296 R501–R511 (2009).
26. Wojaczynski, G. J., Engel, E. A., Steren, K. E., Enquist, L. W. & Patrick Card, J. The neuroinvasive profiles of H129 (herpes simplex virus type 1) recombinants with putative anterograde-only transneuronal spread properties. *Brain Struct. Funct.* **220**, 1395–1420 (2015).
27. Su, P. *et al.* Evaluation of retrograde labeling profiles of HSV1 H129 anterograde tracer. *J. Chem. Neuroanat.* **100**, 101662 (2019).
28. Winnubst, J. *et al.* Reconstruction of 1,000 Projection Neurons Reveals New Cell Types and Organization of Long-Range Connectivity in the Mouse Brain. *Cell* **179**, 268–281.e13 (2019).
29. Gao, Z. *et al.* A cortico-cerebellar loop for motor planning. *Nature* **563**, 113–116 (2018).
30. Jones, E. G. *The Thalamus*. (Springer Science & Business Media, 2012).
31. Sieveritz, B., García-Muñoz, M. & Arbuthnott, G. W. Thalamic afferents to prefrontal cortices from ventral motor nuclei in decision-making. *Eur. J. Neurosci.* **49**, 646–657 (2019).
32. Aumann, T. D., Rawson, J. A., Finkelstein, D. I. & Horne, M. K. Projections from the lateral and interposed cerebellar nuclei to the thalamus of the rat: a light and electron microscopic study using single and double anterograde labelling. *J. Comp. Neurol.* **349**, 165–181

(1994).

33. Ossowska, K. Zona incerta as a therapeutic target in Parkinson's disease. *J. Neurol.* **267**, 591–606 (2020).
34. Mitchell, A. & Chakraborty, S. What does the mediodorsal thalamus do? *Front. Syst. Neurosci.* **7**, 37 (2013).
35. Hunnicutt, B. J. *et al.* A comprehensive thalamocortical projection map at the mesoscopic level. *Nat. Neurosci.* **17**, 1276–1285 (2014).
36. Courchesne, E., Yeung-Courchesne, R., Press, G. A., Hesselink, J. R. & Jernigan, T. L. Hypoplasia of cerebellar vermal lobules VI and VII in autism. *N. Engl. J. Med.* **318**, 1349–1354 (1988).
37. Tervo, D. G. R. *et al.* A Designer AAV Variant Permits Efficient Retrograde Access to Projection Neurons. *Neuron* **92**, 372–382 (2016).
38. Klapoetke, N. C. *et al.* Independent optical excitation of distinct neural populations. *Nat. Methods* **11**, 338–346 (2014).
39. Cavdar, S. *et al.* Cerebellar connections to the rostral reticular nucleus of the thalamus in the rat. *J. Anat.* **201**, 485–491 (2002).
40. Chan-Palay, V. *Cerebellar Dentate Nucleus: Organization, Cytology and Transmitters*. (Springer, 2013).
41. Nakamura, H. Cerebellar projections to the ventral lateral geniculate nucleus and the thalamic reticular nucleus in the cat. *J. Neurosci. Res.* **96**, 63–74 (2018).
42. Watabe-Uchida, M., Zhu, L., Ogawa, S. K., Vamanrao, A. & Uchida, N. Whole-brain mapping of direct inputs to midbrain dopamine neurons. *Neuron* **74**, 858–873 (2012).
43. Phillipson, O. T. Afferent projections to the ventral tegmental area of Tsai and interfascicular nucleus: a horseradish peroxidase study in the rat. *J. Comp. Neurol.* **187**, 117–143 (1979).
44. Carta, I., Chen, C. H., Schott, A. L., Dorizan, S. & Khodakhah, K. Cerebellar modulation of

the reward circuitry and social behavior. *Science* **363**, (2019).

45. Snider, R. S. & Maiti, A. Cerebellar contributions to the Papez circuit. *J. Neurosci. Res.* **2**, 133–146 (1976).
46. Bostan, A. C. & Strick, P. L. The basal ganglia and the cerebellum: nodes in an integrated network. *Nat. Rev. Neurosci.* **19**, 338–350 (2018).
47. Stamatakis, A. M. *et al.* Lateral Hypothalamic Area Glutamatergic Neurons and Their Projections to the Lateral Habenula Regulate Feeding and Reward. *J. Neurosci.* **36**, 302–311 (2016).
48. Mitrofanis, J. & deFonseka, R. Organisation of connections between the zona incerta and the interposed nucleus. *Anat. Embryol.* **204**, 153–159 (2001).
49. Jones, E. G. & Burton, H. Areal differences in the laminar distribution of thalamic afferents in cortical fields of the insular, parietal and temporal regions of primates. *J. Comp. Neurol.* **168**, 197–247 (1976).
50. Jones, E. G. Lamination and differential distribution of thalamic afferents within the sensory-motor cortex of the squirrel monkey. *J. Comp. Neurol.* **160**, 167–203 (1975).
51. Herkenham, M. Laminar organization of thalamic projections to the rat neocortex. *Science* **207**, 532–535 (1980).
52. Thomson, A. M. Neocortical layer 6, a review. *Front. Neuroanat.* **4**, 13 (2010).
53. Hooks, B. M. *et al.* Organization of cortical and thalamic input to pyramidal neurons in mouse motor cortex. *J. Neurosci.* **33**, 748–760 (2013).
54. Llinás, R. R., Leznik, E. & Urbano, F. J. Temporal binding via cortical coincidence detection of specific and nonspecific thalamocortical inputs: A voltage-dependent dye-imaging study in mouse brain slices. *Proc. Natl. Acad. Sci. U. S. A.* **99**, 449–454 (2002).
55. Wiesendanger, R. & Wiesendanger, M. The corticopontine system in the rat. I. Mapping of corticopontine neurons. *J. Comp. Neurol.* **208**, 215–226 (1982).
56. Hashimoto, M. *et al.* Motor and non-motor projections from the cerebellum to rostrocaudally

distinct sectors of the dorsal premotor cortex in macaques. *Eur. J. Neurosci.* **31**, 1402–1413 (2010).

57. Lee, K. H. *et al.* Circuit mechanisms underlying motor memory formation in the cerebellum. *Neuron* **86**, 529–540 (2015).
58. Sakai, S. T. Cerebellar Thalamic and Thalamocortical Projections. in *Handbook of the Cerebellum and Cerebellar Disorders* (eds. Manto, M., Schmahmann, J. D., Rossi, F., Gruol, D. L. & Koibuchi, N.) 529–547 (Springer Netherlands, 2013). doi:10.1007/978-94-007-1333-8_24.
59. Gornati, S. V. *et al.* Differentiating Cerebellar Impact on Thalamic Nuclei. *Cell Rep.* **23**, 2690–2704 (2018).
60. Pinault, D., Smith, Y. & Deschênes, M. Dendrodendritic and axoaxonic synapses in the thalamic reticular nucleus of the adult rat. *J. Neurosci.* **17**, 3215–3233 (1997).
61. Henschke, J. U. & Pakan, J. M. Disynaptic cerebrocerebellar pathways originating from multiple functionally distinct cortical areas. *Elife* **9**, (2020).
62. Yamamuro, K. *et al.* A prefrontal-paraventricular thalamus circuit requires juvenile social experience to regulate adult sociability in mice. *Nat. Neurosci.* **23**, 1240–1252 (2020).
63. Marton, T. F., Seifikar, H., Luongo, F. J., Lee, A. T. & Sohal, V. S. Roles of Prefrontal Cortex and Mediodorsal Thalamus in Task Engagement and Behavioral Flexibility. *J. Neurosci.* **38**, 2569–2578 (2018).
64. Hubel, D. H. & Wiesel, T. N. Binocular interaction in striate cortex of kittens reared with artificial squint. *J. Neurophysiol.* **28**, 1041–1059 (1965).
65. Salgado, S. & Kaplitt, M. G. The Nucleus Accumbens: A Comprehensive Review. *Stereotact. Funct. Neurosurg.* **93**, 75–93 (2015).
66. Küper, M. *et al.* Cerebellar fMRI Activation Increases with Increasing Working Memory Demands. *Cerebellum* **15**, 322–335 (2016).
67. Bohne, P., Schwarz, M. K., Herlitze, S. & Mark, M. D. A New Projection From the Deep

Cerebellar Nuclei to the Hippocampus via the Ventrolateral and Laterodorsal Thalamus in Mice. *Front. Neural Circuits* **13**, 51 (2019).

68. Stoodley, C. J. *et al.* Altered cerebellar connectivity in autism and cerebellar-mediated rescue of autism-related behaviors in mice. *Nat. Neurosci.* **20**, 1744–1751 (2017).
69. Heath, R. G., Dempesy, C. W., Fontana, C. J. & Myers, W. A. Cerebellar stimulation: effects on septal region, hippocampus, and amygdala of cats and rats. *Biol. Psychiatry* **13**, 501–529 (1978).
70. Ozden, I., Dombeck, D. A., Hoogland, T. M., Tank, D. W. & Wang, S. S.-H. Widespread state-dependent shifts in cerebellar activity in locomoting mice. *PLoS One* **7**, e42650 (2012).
71. Apps, R. Gating of climbing fibre input to cerebellar cortical zones. *Prog. Brain Res.* **124**, 201–211 (2000).
72. Ando, N., Izawa, Y. & Shinoda, Y. Relative contributions of thalamic reticular nucleus neurons and intrinsic interneurons to inhibition of thalamic neurons projecting to the motor cortex. *J. Neurophysiol.* **73**, 2470–2485 (1995).
73. Pinto, D. J., Brumberg, J. C. & Simons, D. J. Circuit dynamics and coding strategies in rodent somatosensory cortex. *J. Neurophysiol.* **83**, 1158–1166 (2000).
74. Lam, Y.-W. & Sherman, S. M. Functional organization of the somatosensory cortical layer 6 feedback to the thalamus. *Cereb. Cortex* **20**, 13–24 (2010).
75. Guillery, R. W., Feig, S. L. & Lozsádi, D. A. Paying attention to the thalamic reticular nucleus. *Trends Neurosci.* **21**, 28–32 (1998).
76. Bruno, R. M. & Sakmann, B. Cortex is driven by weak but synchronously active thalamocortical synapses. *Science* **312**, 1622–1627 (2006).
77. Destexhe, A. Modelling corticothalamic feedback and the gating of the thalamus by the cerebral cortex. *J. Physiol. Paris* **94**, 391–410 (2000).
78. Haroian, A. J., Massopust, L. C. & Young, P. A. Cerebellothalamic projections in the rat: an

autoradiographic and degeneration study. *J. Comp. Neurol.* **197**, 217–236 (1981).

79. Faull, R. L. The cerebellofugal projections in the brachium conjunctivum of the rat. II. The ipsilateral and contralateral descending pathways. *J. Comp. Neurol.* **178**, 519–535 (1978).
80. Aumann, T. D. & Horne, M. K. Ramification and termination of single axons in the cerebellothalamic pathway of the rat. *J. Comp. Neurol.* **376**, 420–430 (1996).
81. Card, J. P., Enquist, L. W. & Moore, R. Y. Neuroinvasiveness of pseudorabies virus injected intracerebrally is dependent on viral concentration and terminal field density. *J. Comp. Neurol.* **407**, 438–452 (1999).
82. Shiroyama, T., Kayahara, T., Yasui, Y., Nomura, J. & Nakano, K. Projections of the vestibular nuclei to the thalamus in the rat: a Phaseolus vulgaris leucoagglutinin study. *J. Comp. Neurol.* **407**, 318–332 (1999).
83. Meng, H., May, P. J., Dickman, J. D. & Angelaki, D. E. Vestibular signals in primate thalamus: properties and origins. *J. Neurosci.* **27**, 13590–13602 (2007).
84. Chatterjee, S. *et al.* Nontoxic, double-deletion-mutant rabies viral vectors for retrograde targeting of projection neurons. *Nat. Neurosci.* **21**, 638–646 (2018).
85. Aschauer, D. F., Kreuz, S. & Rumpel, S. Analysis of transduction efficiency, tropism and axonal transport of AAV serotypes 1, 2, 5, 6, 8 and 9 in the mouse brain. *PLoS One* **8**, e76310 (2013).
86. Watakabe, A. *et al.* Comparative analyses of adeno-associated viral vector serotypes 1, 2, 5, 8 and 9 in marmoset, mouse and macaque cerebral cortex. *Neurosci. Res.* **93**, 144–157 (2015).
87. Ugolini, G. Transneuronal transfer of herpes simplex virus type 1 (HSV 1) from mixed limb nerves to the CNS. I. Sequence of transfer from sensory, motor, and sympathetic nerve fibres to the spinal cord. *J. Comp. Neurol.* **326**, 527–548 (1992).
88. Lisberger, S. G. The Rules of Cerebellar Learning: Around the Ito Hypothesis. *Neuroscience* (2020) doi:10.1016/j.neuroscience.2020.08.026.

89. Schmahmann, J. D. & Sherman, J. C. The cerebellar cognitive affective syndrome. *Brain* **121**, 561–579 (1998).

90. Smith, B. N. *et al.* Pseudorabies virus expressing enhanced green fluorescent protein: A tool for in vitro electrophysiological analysis of transsynaptically labeled neurons in identified central nervous system circuits. *Proc. Natl. Acad. Sci. U. S. A.* **97**, 9264–9269 (2000).

91. Legg, C. R., Mercier, B. & Glickstein, M. Corticopontine projection in the rat: the distribution of labelled cortical cells after large injections of horseradish peroxidase in the pontine nuclei. *J. Comp. Neurol.* **286**, 427–441 (1989).

92. Ray, M., Tang, R., Jiang, Z. & Rotello, V. M. Quantitative tracking of protein trafficking to the nucleus using cytosolic protein delivery by nanoparticle-stabilized nanocapsules. *Bioconjug. Chem.* **26**, 1004–1007 (2015).

93. Conte, W. L., Kamishina, H. & Reep, R. L. Multiple neuroanatomical tract-tracing using fluorescent Alexa Fluor conjugates of cholera toxin subunit B in rats. *Nat. Protoc.* **4**, 1157–1166 (2009).

94. Ugolini, G., Kuypers, H. G. & Simmons, A. Retrograde transneuronal transfer of herpes simplex virus type 1 (HSV 1) from motoneurones. *Brain Res.* **422**, 242–256 (1987).

95. Callaway, E. M. Transneuronal circuit tracing with neurotropic viruses. *Curr. Opin. Neurobiol.* **18**, 617–623 (2008).

96. Granstedt, A. E., Bosse, J. B., Thiberge, S. Y. & Enquist, L. W. In vivo imaging of alphaherpesvirus infection reveals synchronized activity dependent on axonal sorting of viral proteins. *Proc. Natl. Acad. Sci. U. S. A.* **110**, E3516–25 (2013).

97. Miranda-Saksena, M., Denes, C. E., Diefenbach, R. J. & Cunningham, A. L. Infection and Transport of Herpes Simplex Virus Type 1 in Neurons: Role of the Cytoskeleton. *Viruses* **10**, (2018).

98. Saleeba, C., Dempsey, B., Le, S., Goodchild, A. & McMullan, S. A Student's Guide to

Neural Circuit Tracing. *Front. Neurosci.* **13**, 897 (2019).

99. Ugolini, G. Advances in viral transneuronal tracing. *J. Neurosci. Methods* **194**, 2–20 (2010).

100. Card, J. P., Enquist, L. W., Miller, A. D. & Yates, B. J. Differential tropism of pseudorabies virus for sensory neurons in the cat. *J. Neurovirol.* **3**, 49–61 (1997).

101. Garner, J. A. & LaVail, J. H. Differential anterograde transport of HSV type 1 viral strains in the murine optic pathway. *J. Neurovirol.* **5**, 140–150 (1999).

102. Bria, A. & Iannello, G. TeraStitcher - a tool for fast automatic 3D-stitching of teravoxel-sized microscopy images. *BMC Bioinformatics* **13**, 316 (2012).

103. Renier, N. *et al.* iDISCO: a simple, rapid method to immunolabel large tissue samples for volume imaging. *Cell* **159**, 896–910 (2014).

104. Shamonin, D. P. *et al.* Fast parallel image registration on CPU and GPU for diagnostic classification of Alzheimer's disease. *Front. Neuroinform.* **7**, 50 (2013).

105. Klein, S., Staring, M., Murphy, K., Viergever, M. A. & Pluim, J. P. W. elastix: a toolbox for intensity-based medical image registration. *IEEE Trans. Med. Imaging* **29**, 196–205 (2010).

106. Klein, S. & Staring, M. Image registration. in *Elastix, the manual* 13–16 (2015).

107. Yoo, A. B., Jette, M. A. & Grondona, M. SLURM: Simple Linux Utility for Resource Management. in *Job Scheduling Strategies for Parallel Processing* 44–60 (Springer Berlin Heidelberg, 2003). doi:10.1007/10968987_3.

108. Allen Institute for BrainScience. Technical white paper informatics data processing for the allen developing mouse brain atlas. (2012).

109. Schmid, B., Schindelin, J., Cardona, A., Longair, M. & Heisenberg, M. A high-level 3D visualization API for Java and ImageJ. *BMC Bioinformatics* **11**, 274 (2010).

110. Sergejeva, M. *et al.* Anatomical landmarks for registration of experimental image data to volumetric rodent brain atlasing templates. *J. Neurosci. Methods* **240**, 161–169 (2015).

111. Seabold, S. & Perktold, J. Statsmodels: Econometric and statistical modeling with python. in *Proceedings of the 9th Python in Science Conference* vol. 57 61 (Scipy, 2010).

112. Roosendaal, T. & Selleri, S. *The Official Blender 2.3 guide: free 3D creation suite for modeling, animation, and rendering*. vol. 3 (No Starch Press San Francisco, CA, 2004).

113. Jones, E., Oliphant, T. & Peterson, P. {SciPy}: Open source scientific tools for {Python}. (2001--).

114. Chen, S., Yang, M., Miselis, R. R. & Aston-Jones, G. Characterization of transsynaptic tracing with central application of pseudorabies virus. *Brain Res.* **838**, 171–183 (1999).

115. Aston-Jones, G. & Card, J. P. Use of pseudorabies virus to delineate multisynaptic circuits in brain: opportunities and limitations. *J. Neurosci. Methods* **103**, 51–61 (2000).

116. van der Walt, S. *et al.* scikit-image: image processing in Python. *PeerJ* **2**, e453 (2014).

117. Lee, K., Zung, J., Li, P., Jain, V. & Sebastian Seung, H. Superhuman Accuracy on the SNEMI3D Connectomics Challenge. *arXiv [cs.CV]* (2017).

118. Gornet, J. *et al.* Reconstructing neuronal anatomy from whole-brain images. in (2019).

119. Goutte, C. & Gaussier, E. A Probabilistic Interpretation of Precision, Recall and F-Score, with Implication for Evaluation. in *Advances in Information Retrieval* 345–359 (Springer Berlin Heidelberg, 2005). doi:10.1007/978-3-540-31865-1_25.

120. Yao, B., Yang, X. & Zhu, S.-C. Introduction to a Large-Scale General Purpose Ground Truth Database: Methodology, Annotation Tool and Benchmarks. in *Energy Minimization Methods in Computer Vision and Pattern Recognition* 169–183 (Springer Berlin Heidelberg, 2007). doi:10.1007/978-3-540-74198-5_14.

121. DeKosky, S. T. & Scheff, S. W. Synapse loss in frontal cortex biopsies in Alzheimer's disease: correlation with cognitive severity. *Ann. Neurol.* **27**, 457–464 (1990).

122. Martinez, M., Calvo-Torrent, A. & Herbert, J. Mapping brain response to social stress in rodents with c-fos expression: a review. *Stress* **5**, 3–13 (2002).

123. Barski, J. J., Dethleffsen, K. & Meyer, M. Cre recombinase expression in cerebellar Purkinje cells. *Genesis* **28**, 93–98 (2000).

124. Kloth, A. D. *et al.* Cerebellar associative sensory learning defects in five mouse autism

models. *Elife* **4**, e06085 (2015).

125. Oliphant, T. E. Guide to NumPy. (2006).

126. McKinney, W. & Others. Data structures for statistical computing in python. in *Proceedings of the 9th Python in Science Conference* vol. 445 51–56 (Austin, TX, 2010).

127. Hunter, J. D. Matplotlib: A 2D Graphics Environment. *Comput. Sci. Eng.* **9**, 90–95 (2007).

128. Waskom, M. *et al. seaborn: v0.5.0 (November 2014)*. (2014). doi:10.5281/zenodo.12710.

129. Lowekamp, B. C., Chen, D. T., Ibáñez, L. & Blezek, D. The Design of SimpleITK. *Front. Neuroinform.* **7**, 45 (2013).

130. Pedregosa, F. *et al.* Scikit-learn: Machine Learning in Python. *J. Mach. Learn. Res.* **12**, 2825–2830 (2011).

131. van Groen, T., Kadish, I. & Michael Wyss, J. Role of the anterodorsal and anteroventral nuclei of the thalamus in spatial memory in the rat. *Behav. Brain Res.* **132**, 19–28 (2002).

132. Wang, C. C. & Shyu, B. C. Differential projections from the mediodorsal and centrolateral thalamic nuclei to the frontal cortex in rats. *Brain Res.* **995**, 226–235 (2004).

133. Bezdudnaya, T. & Keller, A. Laterodorsal nucleus of the thalamus: A processor of somatosensory inputs. *J. Comp. Neurol.* **507**, 1979–1989 (2008).

134. Allen, A. E., Procyk, C. A., Howarth, M., Walmsley, L. & Brown, T. M. Visual input to the mouse lateral posterior and posterior thalamic nuclei: photoreceptive origins and retinotopic order. *J. Physiol.* **594**, 1911–1929 (2016).

135. Matsumoto, M. & Hikosaka, O. Representation of negative motivational value in the primate lateral habenula. *Nat. Neurosci.* **12**, 77–84 (2009).

136. Lee, H. W., Yang, S. H., Kim, J. Y. & Kim, H. The Role of the Medial Habenula Cholinergic System in Addiction and Emotion-Associated Behaviors. *Front. Psychiatry* **10**, 100 (2019).

137. Brown, H. D., Baker, P. M. & Ragozzino, M. E. The parafascicular thalamic nucleus concomitantly influences behavioral flexibility and dorsomedial striatal acetylcholine output in rats. *J. Neurosci.* **30**, 14390–14398 (2010).

138. Kirouac, G. J. Placing the paraventricular nucleus of the thalamus within the brain circuits that control behavior. *Neurosci. Biobehav. Rev.* **56**, 315–329 (2015).

139. Gauriau, C. & Bernard, J.-F. Posterior triangular thalamic neurons convey nociceptive messages to the secondary somatosensory and insular cortices in the rat. *J. Neurosci.* **24**, 752–761 (2004).

140. Casas-Torremocha, D., Clascá, F. & Núñez, Á. Posterior Thalamic Nucleus Modulation of Tactile Stimuli Processing in Rat Motor and Primary Somatosensory Cortices. *Front. Neural Circuits* **11**, 69 (2017).

141. Dolleman-van der Weel, M. J. *et al.* The nucleus reuniens of the thalamus sits at the nexus of a hippocampus and medial prefrontal cortex circuit enabling memory and behavior. *Learn. Mem.* **26**, 191–205 (2019).

142. Tham, W. W. P., Stevenson, R. J. & Miller, L. A. The functional role of the medio dorsal thalamic nucleus in olfaction. *Brain Res. Rev.* **62**, 109–126 (2009).

143. Jankowski, M. M. *et al.* The anterior thalamus provides a subcortical circuit supporting memory and spatial navigation. *Front. Syst. Neurosci.* **7**, 45 (2013).

144. Starr, M. S. & Summerhayes, M. Role of the ventromedial nucleus of the thalamus in motor behaviour--II. Effects of lesions. *Neuroscience* **10**, 1171–1183 (1983).

145. Vertes, R. P., Linley, S. B., Groenewegen, H. J. & Witter, M. P. Chapter 16 - Thalamus. in *The Rat Nervous System (Fourth Edition)* (ed. Paxinos, G.) 335–390 (Academic Press, 2015). doi:10.1016/B978-0-12-374245-2.00016-4.

146. Harrington, M. E. The ventral lateral geniculate nucleus and the intergeniculate leaflet: interrelated structures in the visual and circadian systems. *Neurosci. Biobehav. Rev.* **21**, 705–727 (1997).

147. McGovern, A. E., Davis-Poynter, N., Farrell, M. J. & Mazzone, S. B. Transneuronal tracing of airways-related sensory circuitry using herpes simplex virus 1, strain H129. *Neuroscience* vol. 207 148–166 (2012).

148. McGovern, A. E. *et al.* Anterograde neuronal circuit tracing using a genetically modified herpes simplex virus expressing EGFP. *J. Neurosci. Methods* **209**, 158–167 (2012).

149. Lo, L. & Anderson, D. J. A Cre-dependent, anterograde transsynaptic viral tracer for mapping output pathways of genetically marked neurons. *Neuron* **72**, 938–950 (2011).